National Aeronautics and
Space Administration

Dryden Flight Research Center
P.O. Box 273
Edwards, California 93523-0273

Reply to Attn of: F-96-36/D-1048

Sept. 23, 1996

TO: All Holders of NASA CR-186037, Dated September 1996

FROM: F/Senior Technical Reports Editor

SUBJ: Errata Sheet for NASA CR-186037, Dated September 1996

The subject document has been incorrectly numbered. The correct document number is NASA CR-198053. The correct bibliographic information for this document is as follows:

Norby, W.P., J.A. Ladd, and A.J. Yuhas, *Dynamic Inlet Distortion Prediction with a Combined Computational Fluid Dynamics and Distortion Synthesis Approach*, NASA CR-198053, Sept. 1996.

Your assistance in making the following changes to this document would be greatly appreciated:

1. Use a pen-and-ink change to correct the document number on the cover, title page, and Report Documentation Page.

   - Delete NASA CR-186037
   - Insert NASA CR-198053

2. Staple this Errata Sheet to the document, and ensure that a copy of this sheet is attached to any copies of this document that you distribute.

Thank you for your cooperation. Please call me at (805) 258-2041 if you have any questions.

Camilla F. McArthur

NASA Contractor Report 198053

Dynamic Inlet Distortion Prediction with a Combined Computational Fluid Dynamics and Distortion Synthesis Approach

W.P Norby, J.A. Ladd, and A.J. Yuhas

NASA Contract NAS 3-26617
September 1996

National Aeronautics and
Space Administration

DYNAMIC INLET DISTORTION PREDICTION WITH A COMBINED COMPUTATIONAL FLUID DYNAMICS AND DISTORTION SYNTHESIS APPROACH

W. P. Norby[†], J. A. Ladd[†]
McDonnell Douglas Corporation
St. Louis MO

and

A. J. Yuhas[‡]
AS&M, Inc.
NASA Dryden Flight Research Center
Edwards CA

ABSTRACT

A procedure has been developed for predicting peak dynamic inlet distortion. This procedure combines Computational Fluid Dynamics (CFD) and distortion synthesis analysis to obtain a prediction of peak dynamic distortion intensity and the associated instantaneous total pressure pattern. A prediction of the steady state total pressure pattern at the Aerodynamic Interface Plane is first obtained using an appropriate CFD flow solver. A corresponding inlet turbulence pattern is obtained from the CFD solution via a correlation linking root mean square (RMS) inlet turbulence to a formulation of several CFD parameters representative of flow turbulence intensity. This correlation was derived using flight data obtained from the NASA High Alpha Research Vehicle flight test program and several CFD solutions at conditions matching the flight test data. A distortion synthesis analysis is then performed on the predicted steady state total pressure and RMS turbulence patterns to yield a predicted value of dynamic distortion intensity and the associated instantaneous total pressure pattern.

NOMENCLATURE

a	Acoustic velocity, ft/s
C	Proportionality constant
D_2	Simple distortion intensity descriptor, e.g. $(P_{t\,max}-P_{t\,min})/P_{t\,avg}$
g_c	Proportionality constant for Newton's second law
i	Instantaneous parameter or summation index (subscript)
k	Turbulent kinetic energy, ft^2/s^2
N	Total number of data samples in a population
P_r	Prandtl number
P_{rt}	Turbulent Prandtl number
P_t	Total pressure, psia

[†] Senior Project Engineer, McDonnell Douglas Aerospace, St. Louis, Missouri
[‡] Senior Propulsion Research Engineer

$P_{t\,avg}$	Average AIP total pressure, psia
$P_{t\,i}$	Instantaneous total pressure, psia
$P_{t\,max}$	Maximum AIP total pressure, psia
$P_{t\,min}$	Minimum AIP total pressure, psia
$P_{t\,RMS}$	RMS of total pressure time trace, psia
$P_{t\,ss}$	Steady state total pressure, psia
$P/P_{t\,o}$	Static pressure normalized by freestream total pressure
Turb	Inlet RMS Turbulence
u	Mean flow velocity in axial direction, ft/s
u'	Fluctuating flow velocity in axial direction, ft/s
v	Mean flow velocity in lateral direction, ft/s
v'	Fluctuating flow velocity in lateral direction, ft/s
w	Mean flow velocity in vertical direction, ft/s
w'	Fluctuating flow velocity in vertical direction, ft/s

Greek Symbols

α	Angle of attack, degrees
β	Angle of sideslip, degrees
γ	Ratio of specific heats
ε	Error function or turbulence dissipation rate
ρ	Density, lbm/ft^3
ν	Random number taken from a normal distribution
ω	Ratio of turbulent kinetic energy to turbulent dissipation rate
$\Delta P_{t\,i}$	Fluctuating total pressure component, i.e. $P_{t\,i}$ - $P_{t\,ss}$, psia
$(\Delta P_R/P)_{max}$	GEAE radial distortion intensity distortion descriptor
$(\Delta P/P_c)_{max}$	GEAE circumferential distortion intensity distortion descriptor

Acronyms

AIP	Aerodynamic Interface Plane
CFD	Computational fluid dynamics
CPU	Central Processor Unit
DDS	McDonnell Douglas Dynamic Distortion Synthesis Program
DFRC	Dryden Flight Research Center, Edwards, California
GEAE	General Electric Aircraft Engines, Evandale, Ohio
GMAN	McDonnell Douglas Grid Manager Program
HARV	High Alpha Research Vehicle
HATP	High Alpha Technology Program
LEX	Leading Edge Extension
MDC	McDonnell Douglas Corporation
NASA	National Aeronautics and Space Administration
NASTD	McDonnell Douglas Navier-Stokes Time Dependent Flow Solver Program
PSD	Power Spectral Density
RMS	Root mean square
RNG	Random number generator
SST	Shear stress transport (i.e., Menter turbulence model)
SPS	Samples per second
VG	Vortex Generator
ZONI3G	McDonnell Douglas Zonal Interactive Grid Generation Program

INTRODUCTION

In the development of an air breathing propulsion system, designers seek a high degree of aerodynamic compatibility between the inlet and engine. This is especially true for high performance combat aircraft with high angle of attack maneuvering requirements. The current state-of-the-art process to achieve inlet/engine compatibility involves several extensive inlet and engine test programs and close interaction between the airframe and engine companies. These tests separately determine inlet distortion generation and engine distortion tolerance characteristics. Understanding of inlet distortion levels is needed at the earliest possible stage of the design process to enable trade studies to be performed. However, no reliable dynamic distortion prediction capability currently exists apart from wind tunnel testing with expensive inlet instrumentation and data processing procedures. Digital distortion analysis techniques are well in hand, but the cost of testing usually prohibits high quality dynamic distortion determination in the conceptual design phase of airframe development.

Methods were developed during the 1970's and 1980's to provide an improved level of predictive capability. These methods, known as distortion synthesis, use a random number process to synthesize the fluctuating component of the instantaneous total pressure from the statistical properties of the inlet pressure data[1]. The instantaneous total pressure is split into two components, the steady state and fluctuating pressure, such that

$$P_{t_i} = P_{t_{ss}} + \Delta P_{t_i} . \tag{1}$$

The fluctuating component has a mean of zero and is assumed to be random, stationary, and normally distributed.

In the synthesis approach, it is usually required to obtain the statistical properties of the pressure data from inlet testing. Specifically, these properties take the form of the mean and the root mean square (RMS) of the time variant pressure data. Once obtained, these properties may be used with a normally distributed random number generator to synthesize a time trace for the fluctuating component. While the mean is used to describe the steady state component, the synthesized time trace will have statistical properties matching the original pressure data under conditions where the above statistical assumptions are valid. Once time traces are obtained, the pressure data is then reduced to obtain peak distortion intensity descriptors. A by-product of this analysis is a prediction of the pattern associated with the predicted peak distortion descriptor. In fact, it is the accurate prediction of this pattern that is a most challenging element of the distortion synthesis approach.

It should be reemphasized that synthesis methods require foreknowledge of the steady state total pressure and RMS turbulence at each probe position. Some type of testing is usually required to obtain these properties.

Modern Computational Fluid Dynamics (CFD) has been under continuous and wide-spread development since the late 1960's. It offers distinctive advantages in that it can be performed at any stage of the airframe development process, and that it provides a complete description of the flowfield throughout the computational domain.

Turbulence modeling remains one of the most significant challenges in CFD. Notable advancements have been made over the past several years, including many formulations of two-equation models. The

turbulent kinetic energy (k) is always specified as one of the dependent variables to provide a velocity scale. A second equation uses the turbulence dissipation rate (ε) or the ratio of k and ε, known as ω, as the other dependent variable to provide a length scale.

A sufficiently accurate CFD solution, using a two-equation turbulence model employing a formulation of k, can be used to obtain the required inputs for a distortion synthesis procedure. This would enable a significant capability in which a prediction of peak dynamic distortion can be obtained prior to costly wind tunnel or flight testing.

An approach employing the above concepts was formulated and evaluated using flight data obtained from NASA's High Alpha Research Vehicle (HARV). The HARV inlet research program has developed a significant inlet distortion database at high angles of attack and is ideal for use in developing new analysis techniques.

HARV INLET RESEARCH PROGRAM

The HARV inlet research program is part of the High Alpha Technology Program (HATP). The HATP was initiated by NASA to accelerate maturation of such developing technologies such as aerodynamics, CFD, controls, and propulsion in the high angle-of-attack flight regime. The HARV aircraft[2] , flown at the NASA Dryden Flight Research Center, was the centerpiece of the program. This flight research vehicle, shown in Figure 1, is a modified preproduction F/A-18A with a paddle thrust-vectoring control system installed at the engine nozzle exhausts. This control system provides the aircraft with the capability to fly at steady aerodynamic conditions up to 70° angle of attack. The HARV inlet research program required this capability to obtain the high quality flight data at high angle of attack.

Figure 1. The NASA/McDonnell Douglas F/A-18A High Angle of Attack Research Vehicle

The HARV inlet research program had a number of objectives related to inlet and engine development for future high α aircraft[3]. One of these objectives was the development and validation of CFD for the

prediction of inlet flowfields and distortion levels. The specific question in this study was "can CFD technology be used to accurately predict inlet distortion characteristics at high angle of attack conditions?"

The CFD objective required that full-scale aircraft inlet measurements be obtained throughout the α range to develop the methodology to perform analysis comparisons. Seventy-nine steady aerodynamic attitude conditions were obtained to meet the overall inlet research objectives[3]. Of these maneuvers, eight conditions at Mach numbers of 0.3 and 0.4 were identified for inlet CFD/synthesis development and analysis. These conditions are shown in Table 1.

Table 1. HARV Flight Conditions Used for CFD Analysis

Case	Mach	α (°)	β (°)
1	0.40	4	0
2	0.39	10	0
3	0.40	20	0
4	0.40	39	0
5	0.40	29	0
6	0.31	10	0
7	0.30	20	0
8	0.31	31	0

The aircraft had a separate instrumentation system installed to record inlet measurands. The instrumentation system consisted, primarily, of a 40-probe inlet total pressure rake installed at the AIP directly in front of the starboard engine and wall static pressure ports at the inlet entrance and at the AIP. The rake had dual-measurement ports for low- and high-frequency response pressure measurements with the high-frequency transducers mounted at the port[3]. Figure 2 shows the positions of the rake measurements. The eight low-response wall static pressures at the rake were installed equidistant between each set of rake arms with the ports at the same measurement plane as the rake total pressure measurements. The 19 low-response wall static pressures about the inlet entrance were located in four different circumferential locations. These positions are shown in Figure 3.

The data recording system consisted of PCM modules with signal conditioning and a digital tape recorder. The high-response pressure transducers were absolute pressures and had an onboard anti-aliasing filter applied to the measurement signals. The onboard filter was a six-pole Butterworth low-pass analog filter providing 36 dB per octave rolloff with a nominal cutoff frequency (-3 dB point) of 400 Hz. Digital filtering was applied to the signals during data reduction. The digital filter was a 9-scan rolling window average with a cutoff frequency of 100 Hz. This filter is set to a level consistent with the General Electric F404-GE-400 turbofan engine response to the effects of dynamic distortion.

The low-response pressure transducers were differential pressure measurements with the starboard engine bay pressure used as the reference pressure. The low-response measurements had an in-flight zero calibration capability that allows for zero shift bias error to be removed during post-flight data processing. The high-response pressure transducers had temperature-corrected calibrations applied to their signals during post-flight data processing. Further calibration of these signals was then accomplished using the highly accurate low-response instrumentation. A comparison of the time-averaged levels of the low- and high-response instrumentation at concurrent locations was performed at low distortion conditions prior to the inlet research flight condition being flown. Any bias error between these signals was then removed from the high-response signals. The high response transducers were recorded at a nominal 2143 samples per second (SPS) while the low response was 67 SPS. Additional information on the instrumentation, data recording, and processing system used during the inlet research program is provided in references 3 and 4.

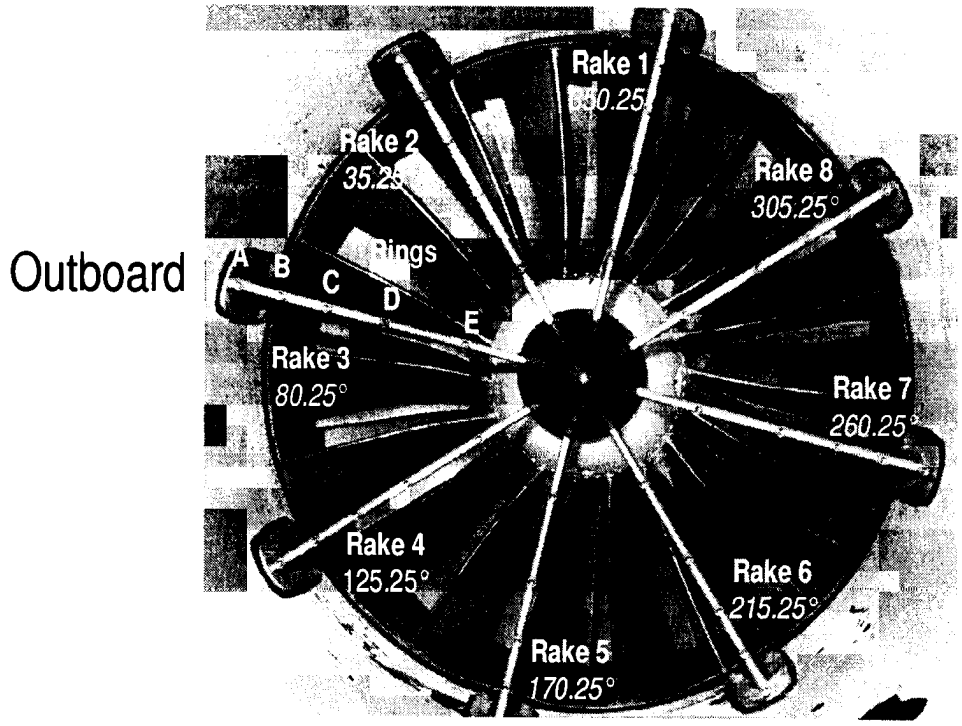

Ring	Immersion From Center*
A	13.223
B	11.670
C	9.876
D	7.674
E	4.498

* inches

Duct Diameter at AIP: 28.7 inches

Figure 2. HARV Flight Test Rake Configuration
Starboard Inlet, View Looking Aft

CFD/SYNTHESIS DYNAMIC DISTORTION MODELING APPROACH

Three distinct elements are required to perform the distortion prediction analysis. The first element is a high order CFD analysis of all regions of the aircraft affecting the flowfield at the inlet/engine AIP. This analysis must be performed using at least a two-equation turbulence model from which inlet turbulence information can be extracted. The results of this analysis will provide flowfield information at the 40 probe positions of the engine face rake. Next, a correlation is needed to convert the results of the turbulence model into equivalent inlet RMS turbulence levels. The process is completed with a distortion synthesis analysis of the steady state and RMS turbulence values at each of the 40 probe positions.

This methodology was developed using flight data from Cases 1 through 4 of Table 1. CFD solutions were obtained for these four cases. A turbulence relationship was developed by correlating a set of CFD computed flowfield parameters back to the measured flight turbulence data. The accuracy of the procedure was then assessed by performing the analysis on Cases 5-8 without foreknowledge of the flight test results. The HARV flight data for these validation cases were used to assess accuracy of the procedure only after the predictions were completed.

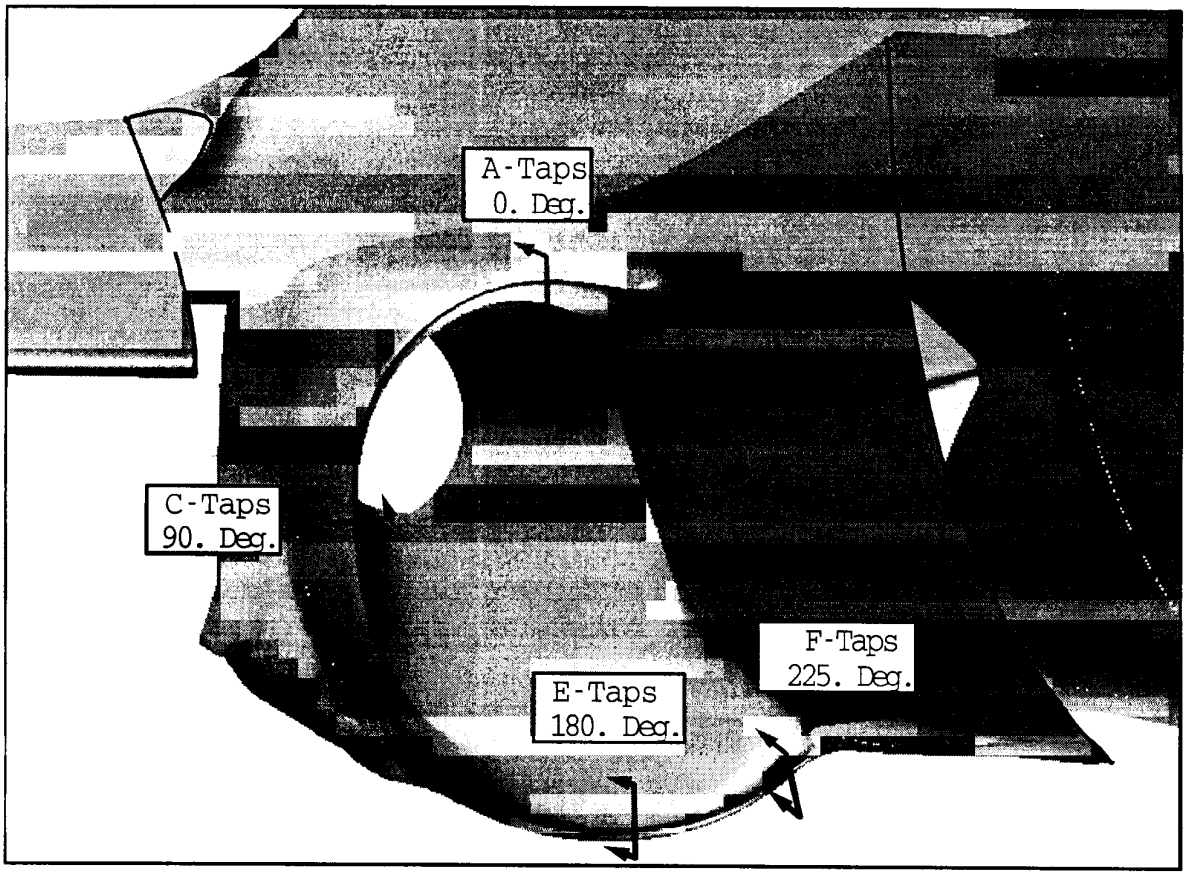

Figure 3. Locations of Inlet Lip Surface Static Pressure Taps

CFD Modeling

Grid Generation

Aerodynamic surfaces for grid generation were obtained from the McDonnell Douglas Corp. (MDC, St. Louis MO) geometry database within the Unigraphics computer aided design system. Analytic surface patches from the design database are converted directly to discrete two-directional surfaces in the MDC ZONal Interactive grid Generation (ZONI3G) program. This program has many geometry manipulating capabilities to generate grid surfaces for structured, unstructured, and Chimera type computations. CFD analyses of the HARV configurations employed a zonal structured grid as well as some grid overlapping (Chimera) in the inlet entrance area as described later in this section. After completion of the zonal surface grid boundaries, the internal mesh and boundary conditions are set using the MDC Grid MANager (GMAN) program. This program provides flexible specification of many different boundary types and checks the grid for anomalies such as negative or zero cell volumes, excessive stretching, and improper boundary coupling. These grid generation tools were used to develop a high quality computational grid for inlet analysis. The surface geometry used for analyses of the HARV configuration is shown in Figure 4. The entire grid system contains twenty-three zone blocks totaling over three million points, half of which are located in the inlet and diffuser regions. A solid sting (not shown) was used aft of the nozzle exits to simulate ideally expanded jet plumes. The vertical and horizontal tails were not modeled since they are far

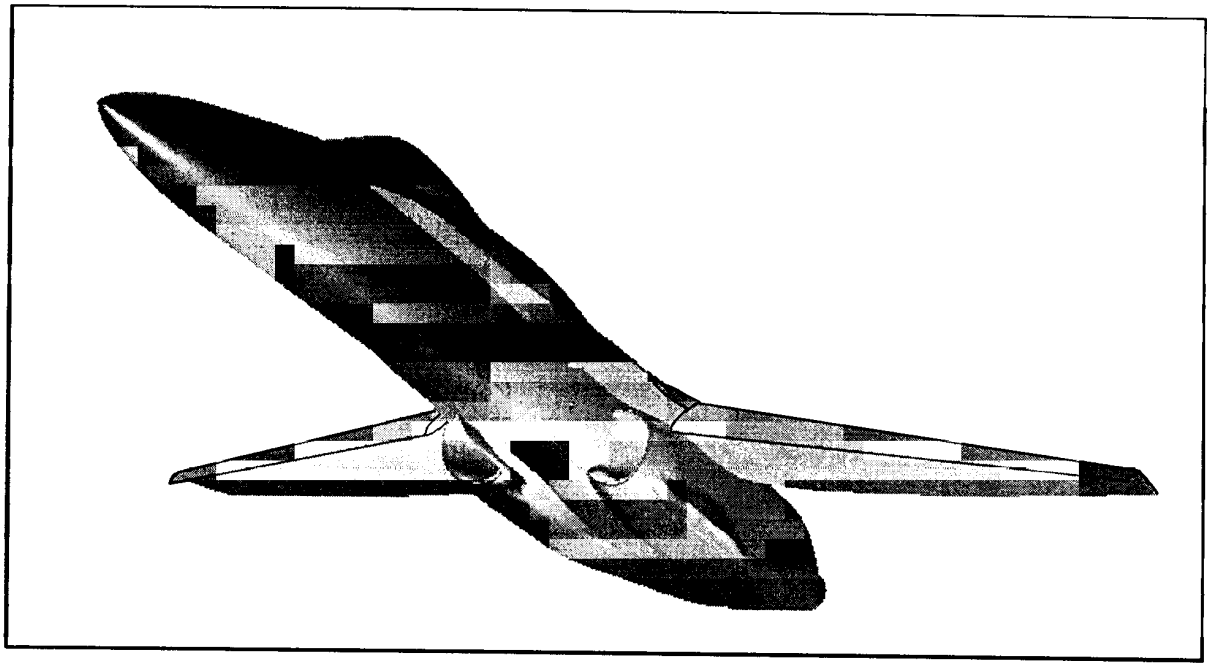

Figure 4. Surface Geometry for HARV CFD Solutions

downstream of the inlet region and do not significantly affect the inlet approach flow. The appropriate leading edge flap deflections were modeled for each angle of attack while trailing edge deflections were omitted. The boundary layer splitter and diverter passages were completely simulated including exhausting the upper diverter passage out to the fuselage upper surface. Boundary layer bleed flow on the splitter surface is believed to be insignificant for the flight conditions considered and so was not simulated. Figure 5 shows the computational grid in the region of the inlet highlight including a C-grid that was used to resolve the high flow gradients around the lower inlet cowl lip. Every other grid point is shown in all figures for clarity.

The single pair of counter-rotating vortex generators (VG's) on the lower surface of the diffuser was simulated using the internal fringe boundary capability of the CFD flow solver. The VG's were modeled as inviscid flat plates that are "carved out" of the internal grid structure as shown in Figure 6. The inviscid assumption of the VG surfaces was not expected to alter the strength or trajectory of the shed vortices since high pressure gradients and flow turning are the primary mechanisms of VG's. Viscous effects from the surfaces of the VG's should be small.

A centerbody was modeled in the grid to simulate the nose cone of the rake assembly and the engine hub. The aft part of the diffuser grid and the assumed centerbody shape is shown in Figure 7. The HARV 40 probe rake is also shown in this figure. At the location of the engine fan face, the centerbody and diffuser duct were extrapolated downstream a distance of three duct diameters. This extrapolation is done to move the constant static pressure boundary condition away from the AIP so that it does not largely influence the natural pressure gradients near the AIP. This is the most common procedure used for the diffuser downstream boundary condition but does not model the presence of the engine as described in the next section.

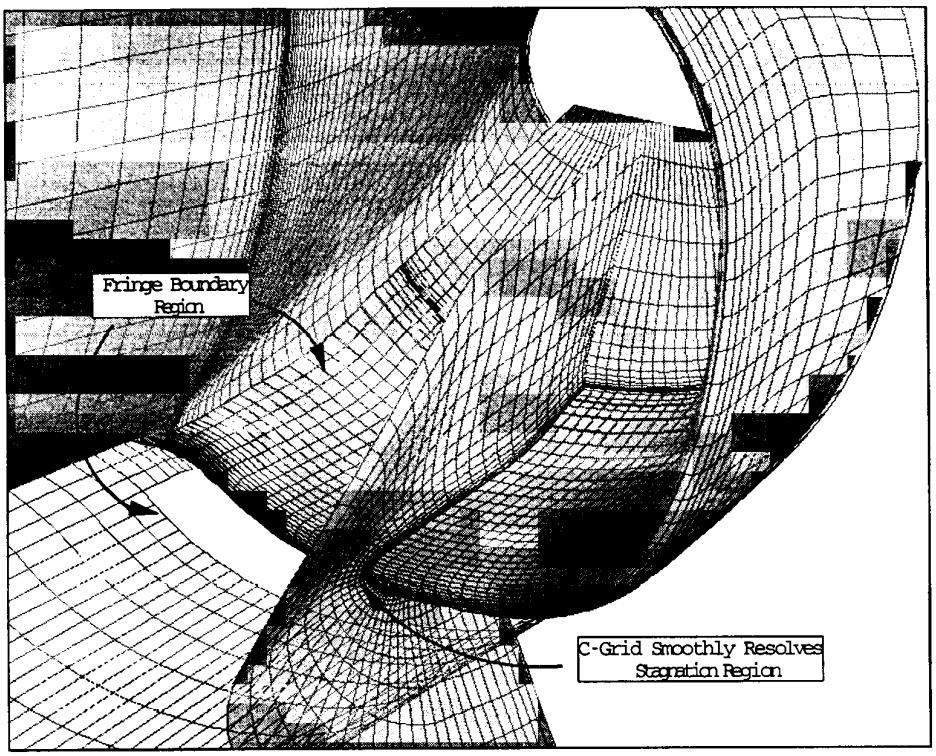

Figure 5. Computational Grid in the Inlet Region

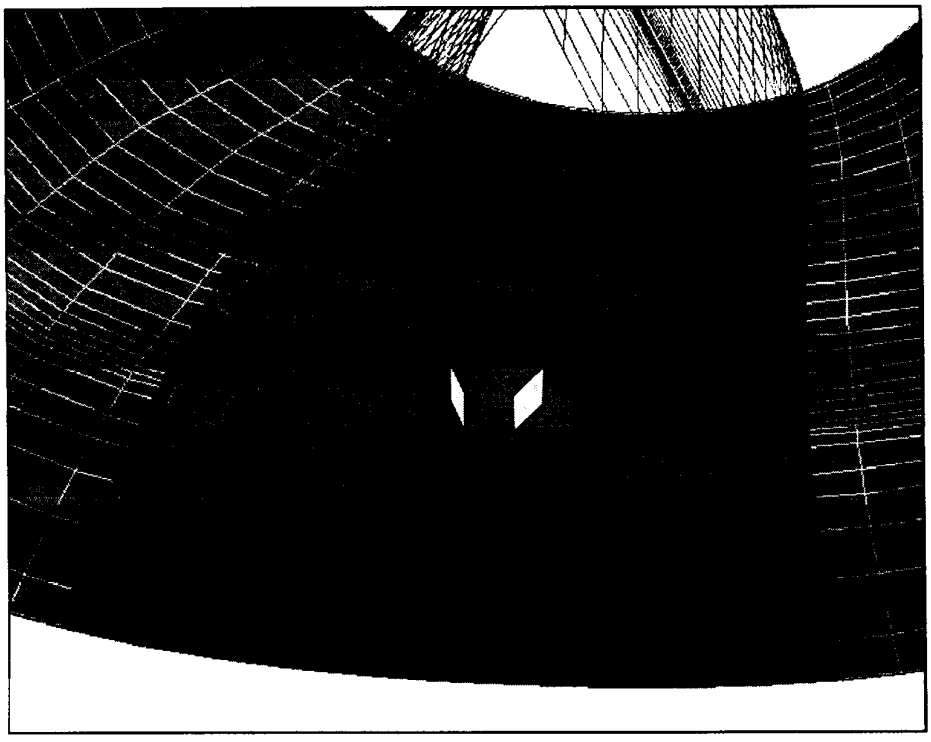

Figure 6. Vortex Generator/Diffuser Grid Topology

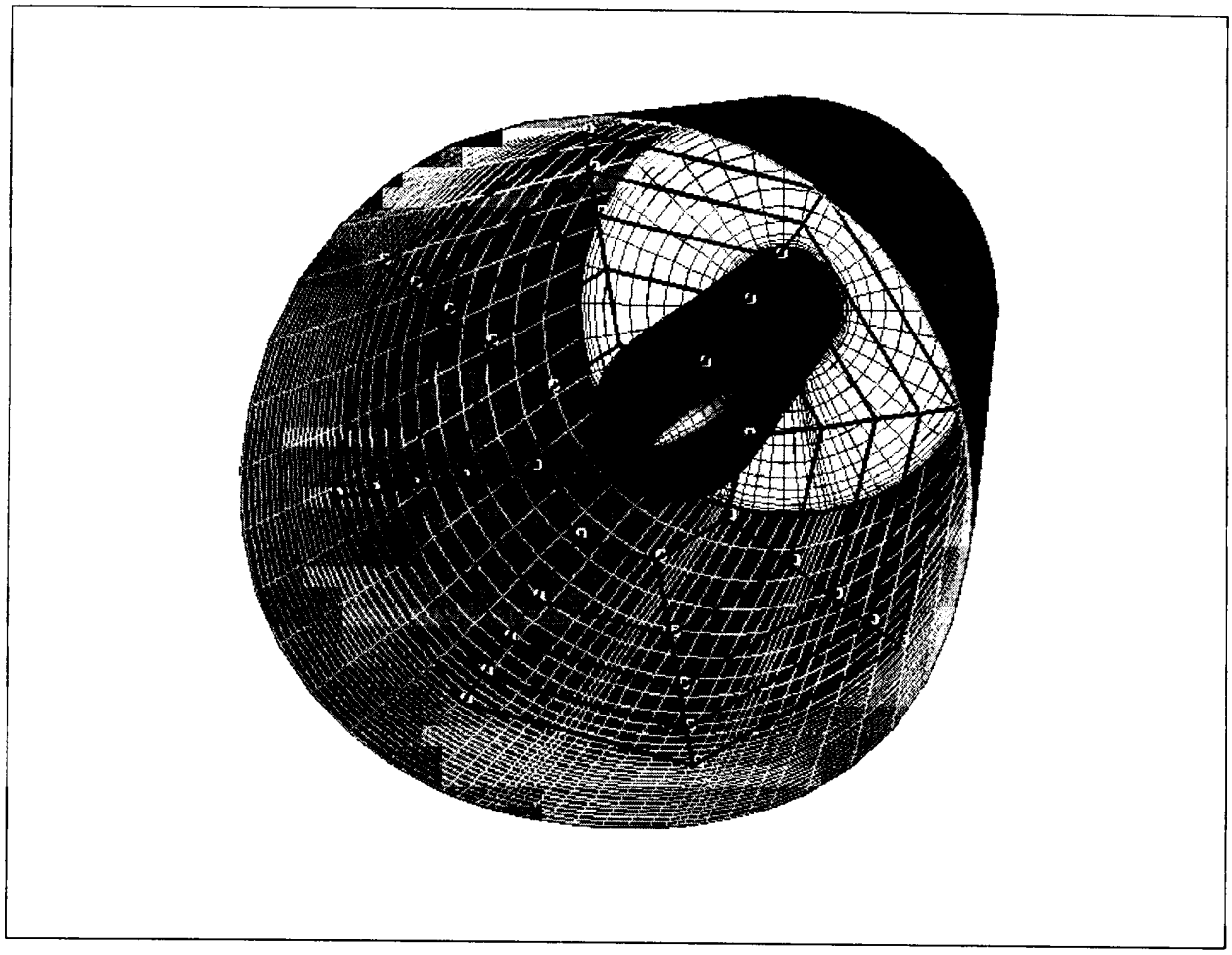

Figure 7. Aft Diffuser Modeling Showing AIP Probe Positions and Centerbody Shape

CFD Analysis Program

The McDonnell Douglas Reynolds-averaged NAvier-Stokes Time Dependent (NASTD) program was used for all computations. Details of the numerical algorithm and solution procedure are outlined by Bush[5]. A recently developed finite volume scheme is employed which results in second order accuracy in physical space. The program has a grid "sequencing" capability in which data are computed only on every other point in any or all of the three grid coordinate directions. This enables the large features of the flowfield to be obtained quickly (eight times as fast as the full grid) before enabling the full grid to resolve the final details of the simulation. Ideal gas is assumed and a Prandtl number of $P_r = 0.72$ and turbulent Prandtl number of $P_{r,t} = 0.9$ are used for all computations. Both the one-equation turbulence model of Spalart and Allmaras[6], and the two-equation Shear Stress Transport (SST) model of Menter[7] were used to obtain steady state flowfield solutions. The SST model was employed for all conditions since the turbulent kinetic energy (k) is required for the calculation of the dynamic distortion. The Spalart and Allmaras turbulence model was used for selected configurations and yielded predictions of total pressure recovery similar to those from the SST model. NASTD solves the turbulence model equations decoupled from the Navier-Stokes equations. The current flowfield variables are used by the turbulence model at each iteration to obtain the eddy viscosity at all points. These values are then used by the mean flow solver to compute new estimates of the conservative variables to give back to the turbulence model iteration. The turbulence models are used in their original form with no modifications.

Menter SST Turbulence Model. Menter's SST model[7] is a variation of a previous model, which accounts for the transport of the principal turbulent shear stress in adverse pressure gradient boundary-layer flows. This model has been found to be very robust and stable for a variety of flow conditions and requires only 10% more computation time than the Spalart one-equation model. This model solves equations for k and ω in the inner region of the boundary layer and gradually changes to the high Reynolds number k-ε model away from the wall. This allows a straightforward Dirichlet[7] boundary condition at the wall for ω, which aids in stability and convergence. Any free shear layers are computed using the k-ε model, which predicts spreading rates more accurately than the k-ω model. The SST model is also formulated so that solutions are independent of the freestream conditions of the turbulent variables. The Boussinesq[7] approximation must be used to obtain closure of the turbulence model equations. This assumption of turbulence isotropy relates the turbulent shear stresses to gradients of the mean velocity field and is perhaps the greatest weakness of all one- and two-equation turbulence models.

Boundary Conditions. All solid surfaces are treated viscously except the VG surfaces and the entire flow is assumed turbulent. Characteristic boundary conditions are assumed at the upstream and outer boundary surfaces. Freestream pressure is assumed at the external outflow boundary located approximately five vehicle lengths downstream. The most difficult boundary condition, and perhaps the most important for inlet flowfields, is the exit of the diffuser. Military power corrected mass flow appropriate for each case is input to the NASTD program. Every five iterations the code drives the corrected mass flow to the specified amount by changing the diffuser downstream static pressure in the appropriate direction. Any effects the presence of the engine has on the approaching flow, such as swirl or pumping, will not be modeled as the downstream pressure is assumed uniform. This boundary condition is believed to be a significant source of error in the simulations, and efforts are currently underway to provide a more realistic simulation of the presence of the engine.

Solution Strategy and Program Requirements. Solution convergence is determined by monitoring the residual errors of the Navier-Stokes and turbulence model equations, engine face contours, average recoveries, and inlet lip surface pressures. The computations were obtained using as many as 20 Hewlett-Packard (Palo Alto, CA) Model 715 and 735 computers running simultaneously on one configuration using a virtual-parallel procedure. The CPU time required by the program using the SST turbulence model is nearly 600 microseconds/iteration/node. Memory required for the full grid simulations is near 80 megabytes. Each simulation typically required 3000 iterations on the sequenced grid plus 500 iterations on the full grid. To the our knowledge, this is the first time such a large scale computational effort has been made using a two-equation turbulence model.

The high angle-of-attack flowfields associated with the HARV flight conditions are inherently unsteady. Because time accurate solutions are impractical, we rely on information from steady state solutions of the Reynolds averaged Navier-Stokes and turbulence equations. There is no guarantee that these steady state solutions will converge to the time average of the unsteady flight data. It is essential, however, that the predicted steady state pattern is as close to the flight data average as possible for the synthesis method to yield accurate estimates of the dynamic distortion parameters.

CFD Results

Several observations can be made from the CFD simulations of the HARV flight conditions and are summarized as follows:

1) $P_{t\,min}$ is consistently predicted to be lower than the flight test data, usually due to the losses from the VG vortices.

2) The mass flow ratios are greater than 1.0 for all cases studied which give rise to local supersonic flow around the lower lip section.

3) Predicted boundary layer separations near the inlet lips were most often consistent with flight test surface pressure data

4) The secondary flow features of the diffuser were strongly affected by the structure of the inlet lip boundary layer separations.

The high angle of attack conditions under study give rise to inherently unsteady aerodynamic flows. The dynamic flowfield and large vortices shed from the leading edge extensions (LEX) are illustrated in Figure 8 for the Case 4 flight condition. Characteristic circular contours of total pressure and spiraling streamlines over the LEX and wing indicate the large scale vortical structures. Part of the centerbody has been removed and the diffuser made transparent to view the total pressure patterns in the duct. There is also an indication of a weak vortex under the LEX, which is eventually ingested by the boundary layer diverter.

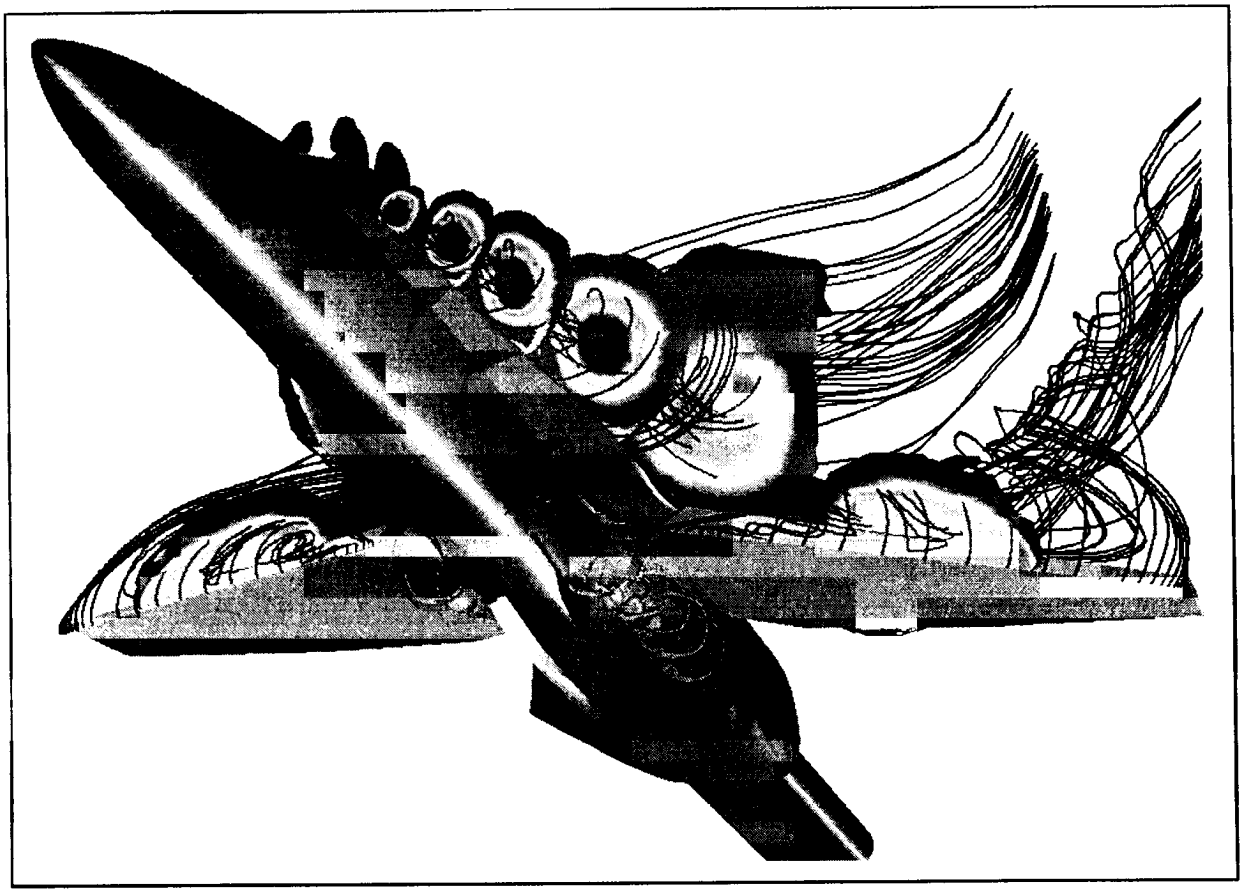

Figure 8. CFD Computed Flowfield Features of the HARV At Angle of Attack
Mach 0.4, α=39°- Case 4

Inlet Lip Surface Pressures. The computed lip surface pressures agreed well with HARV flight test results. Four sections of inlet lip surface pressure taps are available from the HARV data, as shown in Figure 3. The lower inlet lip was designed nearly four times thicker than the upper lip to avoid boundary layer separation at the higher angles of attack. Comparisons between flight test and CFD predicted inlet lip surface pressures for Case 1 (Mach 0.4 and α=3.6°) are shown in Figure 9. The good agreement is typical of all the simulated flight conditions. There are significant pressure gradients around the upper lip sections due to the high mass flow ratio and low angle of attack. Contours of local Mach number are also shown to illustrate the extent of supersonic flow and boundary layer separation. The surface pressure variations and Mach contours from Case 4 (Mach 0.4, α=39°) are shown in Figure 10 and are dramatically different from those at lower angles of attack. There is only a mild amount of flow expansion near the upper inlet entrance, but large regions of very low pressure and supersonic flow are evident near the lower lip. The agreement in this region of high gradients and boundary layer separation is quite good. This is in no doubt due to the deliberately high grid density in this region and a good prediction of the eddy viscosity from the SST turbulence model.

Engine Face Recoveries. The minimum recovery at the AIP, which is an indication of distortion, was consistently underpredicted by the CFD analysis. The large secondary flow features predicted for the Case 3 condition are evident in the contours of diffuser total pressure recovery shown in Figure 11. Disturbances from both the inlet lip separation and the vortex generators are clearly visible. Figure 12 compares steady state recovery on the 40 probe rake as measured from flight test and as interpolated from the CFD solution for the Mach 0.4, α=3.6° Case 1. These contours are shown as they appear at the starboard AIP looking forward. The location of each probe is indicated in the contour plot. The overall average recovery is in excellent agreement, but there are differences in the local distribution of the recovery values. The flight measured data indicate a fairly high level of recovery at the tip of the lowest rake, potentially a benefit from the VG. A fairly low level is indicated from the computation. This can be attributed to the simulation of the VG vortices and/or the downstream boundary condition. The CFD method is overpredicting the losses associated with the VG, or the downstream trajectory is being computed such that the lower rake intersects one of the vortex cores rather than the high recovery trough between the two counter-rotating vortices. The trajectory and strength of the VG vortices are suspected to be significantly altered by the assumption of constant static pressure at the diffuser exit. More rigorous modeling of the effect of the presence of the engine may have a favorable effect on the simulation of the VG vortices. Also, it was later discovered that the VG's in the CFD simulation were placed 2.1 inches inboard of their proper position in the diffuser. Correction of this error may also provide more favorable comparisons.

Several assumptions were made to the geometry and boundary conditions which may significantly affect the CFD predictions of flow quantities at the AIP. The leading edge flap to fuselage junction was not rigorously modeled, which could affect the inlet lip losses. No trailing edge flap was modeled although deflection angles were less than 5 degrees in all cases and should not significantly alter the wing circulation. Differences in the CFD predicted steady state recovery patterns at the AIP are most likely a result of unsatisfactory modeling of the vortex generators and the boundary condition employed at the extended diffuser exit and engine influences at the AIP. In addition to the positioning error, the VG's were modeled as flat plates whereas the actual VG's are 8% thick airfoils. The surfaces of the VG's were assumed inviscid. This is thought to be a good assumption but will be investigated in the follow on task. Figure 12 also shows that the CFD is predicting nearly the right boundary layer thickness around the diffuser duct but that the losses near the wall are larger than the flight data. It is believed that a more accurate modeling of the presence of the engine will have a favorable effect on this behavior. Underprediction of the minimum total pressure gives rise to overprediction of the steady state circumferential and radial distortion.

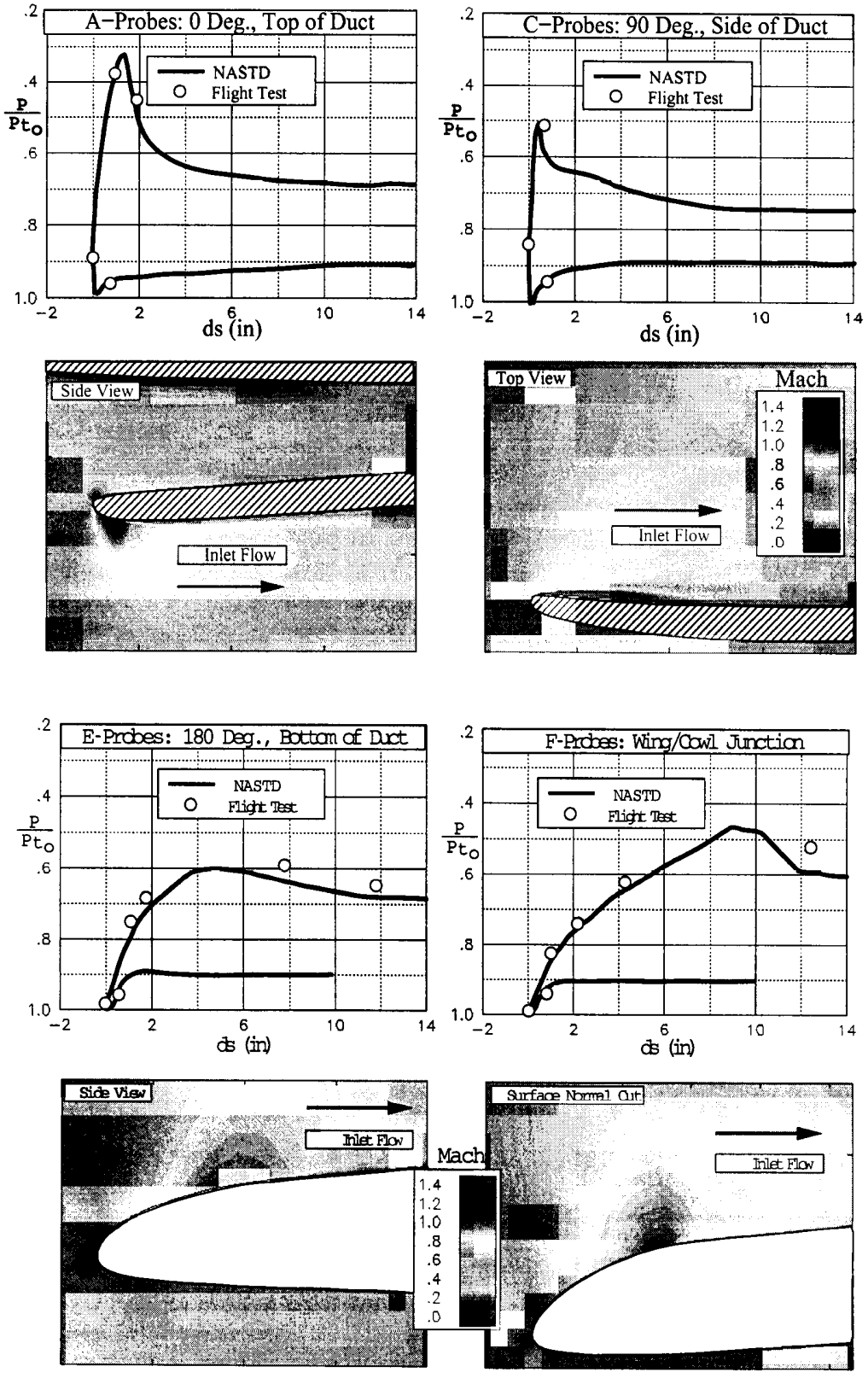

Figure 9. CFD/Flight Inlet Lip Surface Pressure Comparisons at Low Angle of Attack
Mach 0.4, α=3.6° - Case 1

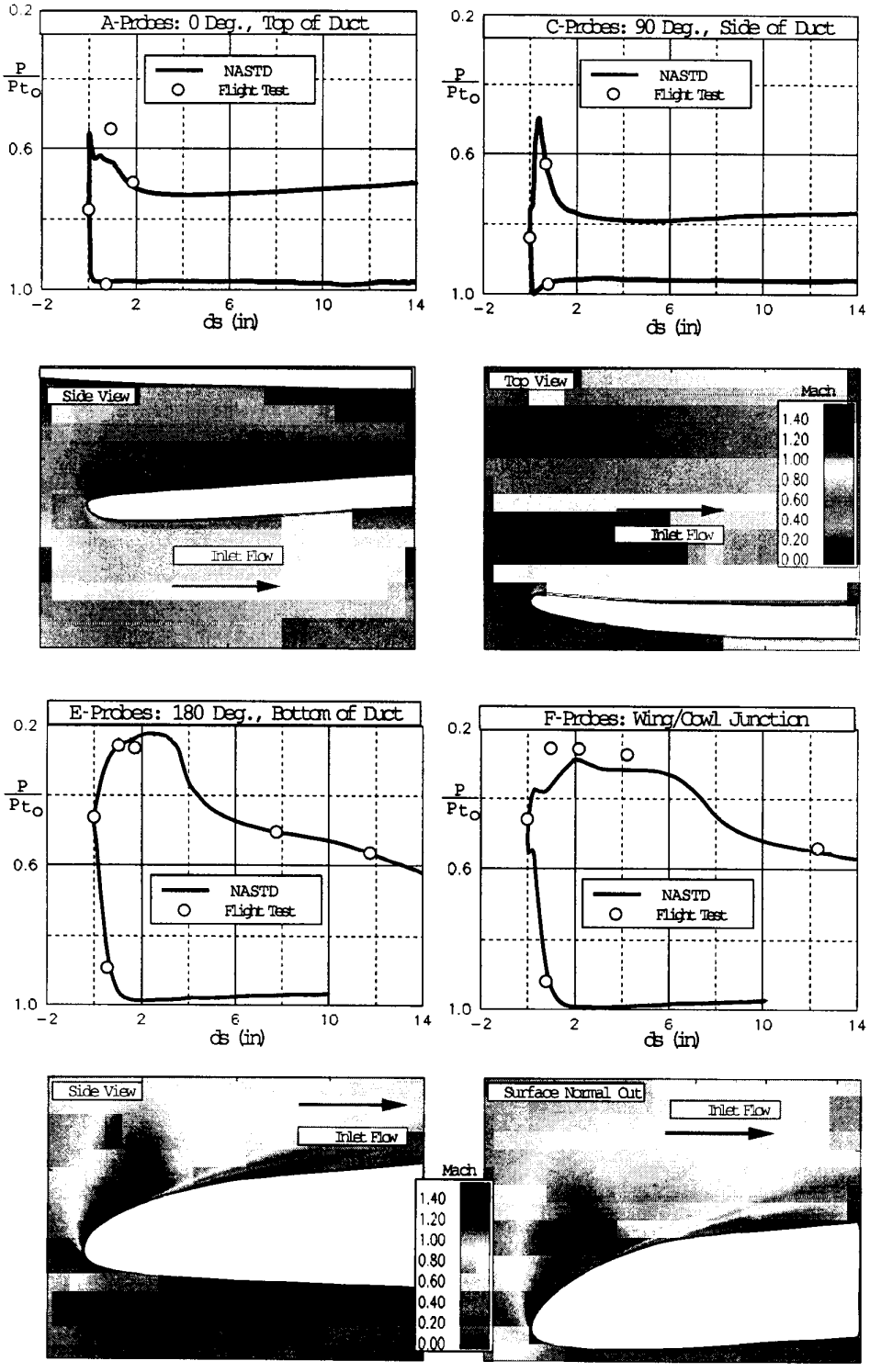

Figure 10. CFD/Flight Inlet Lip Surface Pressure Comparisons at High Angle of Attack
Mach 0.4, α=39° - Case 4

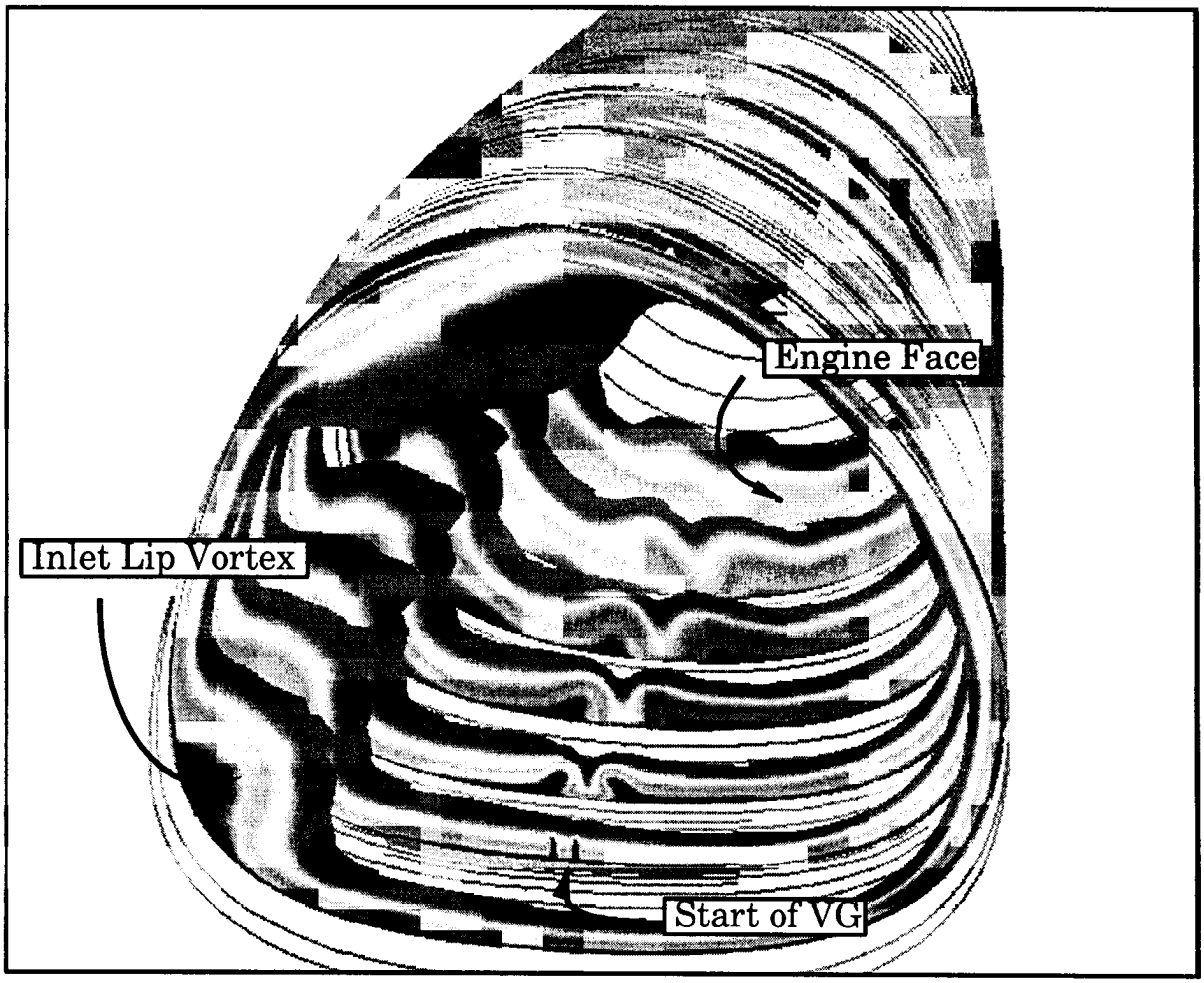

Figure 11. Internal Flow Features of the F/A-18A HARV Diffuser
Mach 0.4, α=20° - Case 3

The AIP pattern is much more dynamic at high angle of attack. As indicated by the flight test and CFD data for Case 4 shown in Figure 13, there is significant secondary flow in the diffuser. Again, the overall recovery is very well predicted while the details of the pattern are only qualitatively correct. The high losses at the bottom of the duct from the CFD are due to a merger between an inlet lip vortex and the vortices shed from the VG simulation. It is this underprediction of the minimum total pressure that leads to higher steady state distortion than the flight test data.

Turbulence Correlation

The CFD to RMS turbulence correlation should be based on physical fluid dynamic principles and remain consistent with the definition of RMS inlet turbulence. The correlation was derived using Cases 1-4 and made use of flight and CFD computed data. The primary correlating parameter is the turbulent kinetic energy, k.

Turbulent kinetic energy is defined from the velocity fluctuations about the mean velocity in each of the three component directions. Stated mathematically,

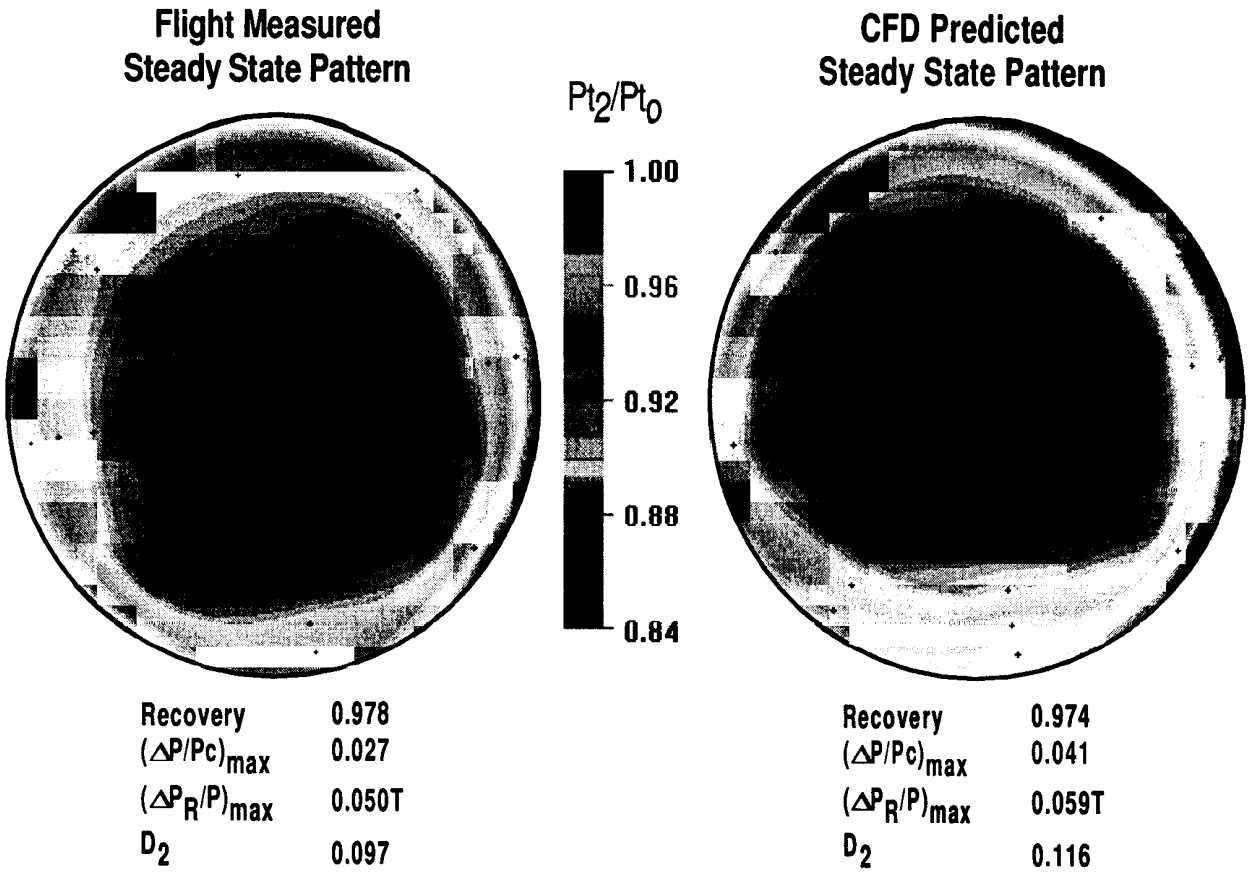

Figure 12. Steady State Total Pressure Recovery Comparisons at Low Angle of Attack
Mach 0.4, α=3.6°, Case 1 - View Looking Forward

$$k = \frac{1}{2}\left(\overline{u'^2} + \overline{v'^2} + \overline{w'^2}\right) \tag{2}$$

The Menter two-equation turbulence model, as well as all two-equation models, assumes the turbulence to be isotropic. This means that the mean turbulent velocity fluctuations are assumed uniform in all directions. Thus, equation (2) can be simplified to,

$$k = \frac{3}{2}\overline{u'^2} \tag{3}$$

Inlet turbulence is defined as the RMS of the total pressure fluctuations at an AIP probe normalized by the average steady state total pressure at the AIP.

$$Turb = \frac{1}{P_{t_{ss}}}\sqrt{\frac{1}{N}\sum_{i=1}^{N}\left(P_{t_i} - P_{t_{ss}}\right)^2} \tag{4}$$

From equations (3) and (4) one can see that turbulent kinetic energy is defined in terms of velocity fluctuations, while inlet turbulence is stated in terms of total pressure fluctuations. While these are different parameters, they are related in a fundamental sense. Clearly, an instantaneous fluctuation in

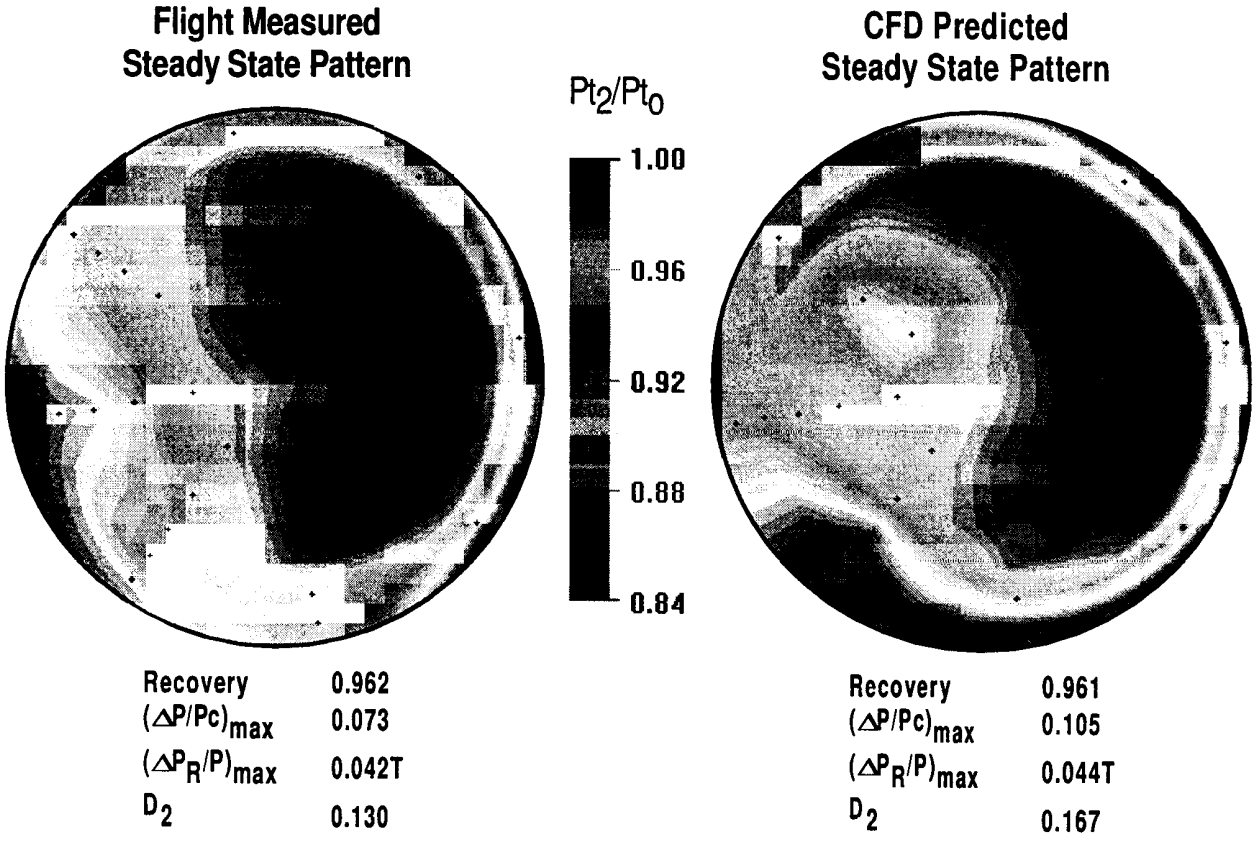

Figure 13. Steady State Total Pressure Recovery Comparisons at High Angle of Attack
Mach 0.4, α=39°, Case 4 - View Looking Forward

velocity will result in a corresponding fluctuation in total pressure. The converse is also true. Thus, one can reasonably expect to find a correlation between RMS turbulence and turbulent kinetic energy.

A potential model equation for the correlation can be obtained by summing the various contributors to pressure fluctuations. The summation yields the following equation as a starting point for the correlation,

$$\frac{Turb \cdot P_t}{\rho} = C_1 k + C_2 (u+a)\sqrt{k} + C_3 (u-a)\sqrt{k} + C_4 u\sqrt{k} \tag{5}$$

where C_1, C_2, C_3, and C_4 are constants to be determined. The first term represents the contribution from non-linear turbulence modes. This turbulence results from energy extracted from the mean flow into large scale fluctuations and the interaction between the large and small scale turbulent modes. The contributions from this mode are expected to be small compared to other sources. The second and third terms are the contributions from acoustic interaction with the turbulence. Because acoustic interaction is at relatively high frequency compared to engine response, its contribution to inlet turbulence is expected to be insignificant due to the low pass filtering performed on the pressure data prior to RMS turbulence calculation. The fourth term is due to linear convected turbulence. Its source is from major turbulence generators such as lip separation and ingestion of vortices. Therefore, it is expected that this term is the only significant contributor to inlet turbulence that plays a role in inlet/engine compatibility.

Numerical experiments have confirmed that linear convected turbulence is the dominant term. The selected model equation for the correlation is then

$$Turb = \frac{C}{\gamma \cdot g_c} \frac{u\sqrt{k}\rho}{P_t}. \tag{6}$$

In this case, u is the steady state axial, or convective, velocity. This equation is used to compute a predicted value of turbulence based on the CFD predicted values of u, k, ρ, and P_t at each probe position on the AIP. The remaining task is to obtain a suitable numerical value for the proportionality constant C. This is accomplished by the method of least squares.

The proportionality constant is determined by defining an error function from the selected correlation equation. After some rearranging of the total pressure and density terms in equation (6), the error function is defined as,

$$\varepsilon_i = \frac{C}{\gamma \cdot g_c} u_i k_i^{1/2} - \frac{Turb_i \cdot P_{t_i}}{\rho_i}, \tag{7}$$

where $Turb_i$ is an experimentally measured RMS turbulence value at the ith probe and all other subscripted variables are CFD-computed flowfield parameters at the same probe position. We seek to determine the value of C that minimizes the sum of the squares of the error terms. Because the AIP rake contains 40 probes, there are 40 CFD/flight data pairs for each of the cases under study. The number of error terms is 40 times the number of conditions for which flight and CFD data exist. The sum of the squares of the error terms is minimized by taking the first derivative of the sum of the squares with respect to the proportionality constant,

$$\frac{\partial\left(\sum_{i=1}^{N} \varepsilon_i^2\right)}{\partial C} = 0. \tag{8}$$

Here, N represents the total number of data pairs. In this case, four CFD/flight test conditions are to be correlated, so N=160. Substitution of equation (7) into equation (8) and solving for C yields

$$C = \gamma g_c \frac{\sum_{i=1}^{N} \frac{u_i k_i^{1/2} Turb_i P_{t_i}}{\rho_i}}{\sum_{i=1}^{N} u_i^2 k_i}. \tag{9}$$

The procedure to determine the correlation coefficient first begins with obtaining a CFD solution for a number of conditions for which flight or wind tunnel data exist. From the CFD solution, determine u, ρ, P_t, and k at each AIP probe position. Also, obtain the experimentally determined RMS turbulence for each probe position. Finally, accumulate the statistics from the data and compute the correlation coefficient using equation (9).

The results of the correlation process did not result in a robust correlation with the first attempts. Any disagreement, large or small, in the *location* of the total pressure losses at the engine face degraded the quality of the correlation. This means that the magnitude of the total pressure losses *and* the trajectory of these losses must be accurately predicted. For example, if the wake from a separated region impacts the AIP on the third ring from the wall on any particular rake, but the CFD solution predicts it impacting the fourth ring, the procedure described above will attempt to correlate a high turbulence region into a relatively lower turbulence region.

A modified procedure was developed to permit a meaningful correlation to be obtained. This procedure attempts to align high measured values of turbulence with high CFD calculated values of $u \cdot k^{1/2}$. In effect, this removes any consideration of the pattern agreement of the CFD solution to the flight measured turbulence data. It is hoped that future CFD solutions, with enhanced methodology to be described later, will improve the spatial agreement to enable direct correlations. The correlation obtained using the sorting procedure described above is illustrated in Figure 14. The value of the correlation coefficient is approximately 390.5. The correlation yields turbulence values lower than the flight measured data for turbulence levels above 1.3%. It is expected that additional data added to the database will better define the higher turbulence regions of the correlation.

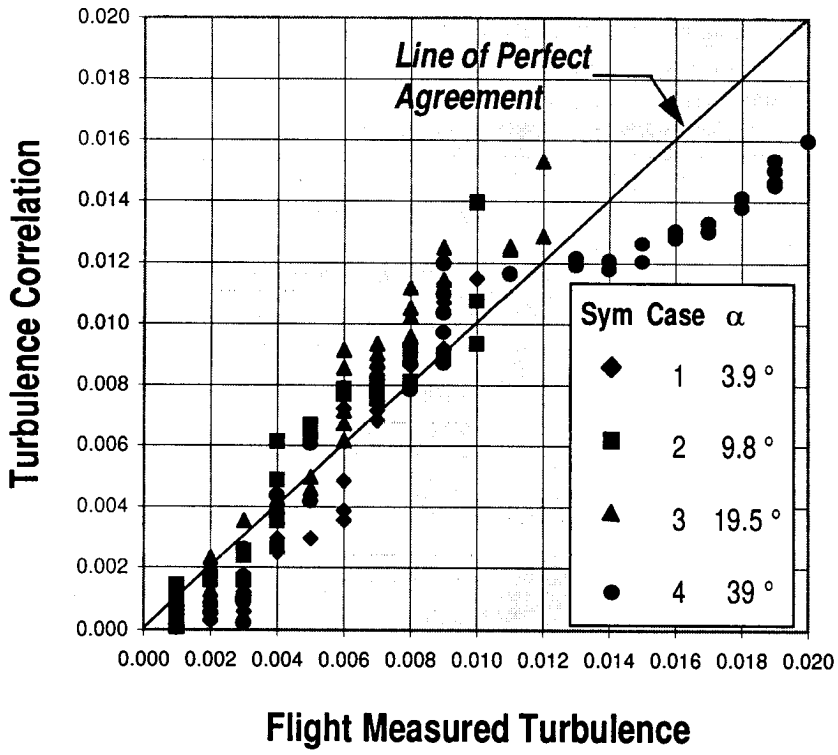

$$Turbulence = \frac{C}{\gamma \cdot g_c} \frac{u\sqrt{k}\rho}{P_t}$$

$$C = 390.523$$

$$\gamma = 1.4$$

$$g_c = 32.174 \frac{ft \cdot lbm}{lb \cdot sec^2}$$

Figure 14. Turbulence Correlation Results Based on Cases 1-4
Mach 0.4 for all Cases

Distortion Synthesis Methodology

The McDonnell Douglas distortion synthesis procedure used for this effort was an existing code. The program, called Dynamic Distortion Synthesizer (DDS), is patterned after that of Sedlock[1]. The starting point for this, and all synthesis routines, is a set of values for the steady state total pressures at each probe with the corresponding RMS turbulence pressures. The general features and characteristics of the code are discussed below.

Random Number Generator

The basis for the synthesis method is that a fluctuating pressure component can be constructed and added to the steady state total pressure. The fluctuating pressure is assumed to be random, stationary, and normally distributed. The synthesized fluctuating pressure for each probe is obtained using a random number generator with a mean of zero. Each "scan" of the synthesized time history for any single probe is constructed using the following expansion of equation (1).

$$\left(\frac{P_t}{P_{t_o}}\right)_i = \left(\frac{P_t}{P_{t_o}}\right)_{ss} + \left(\frac{P_{t_{RMS}}}{P_t}\right)\left(\frac{P_t}{P_{t_o}}\right)_{ss} \nu_i \tag{10}$$

where $(P_t / P_{to})_{ss}$ is the probe's steady state recovery, $(P_{t\,RMS} / P_t)$ is the probe's RMS turbulence, ν is a random number selected from a normal distribution, and the subscript i refers to the ith synthesized scan.

The random number generator used by DDS produces a number from a normal distribution through use of the central limit theorem. This theorem states that sums of independent random variables under general conditions will be normally distributed[8]. The DDS random number generator averages twelve random numbers, taken from an even distribution, to produce a single random number from a normal distribution. The total population of random numbers is scaled such that it has an RMS of 1.0. Thus, the population of all scans computed from the second term of equation (10) will have an RMS equal to the original turbulence value. This ensures consistency between the RMS of the synthesized time traces and the original data.

After synthesis is performed, the time traces are low-pass filtered in a manner consistent with the HARV inlet data filtering. HARV processing procedures use a nine-scan sliding average filter to simulate the effect of a five-pole Bessel filter, the specification low pass filter of the F404-GE-400 engine for distortion calculations. Filtering of the synthesized dynamic data helps impose a degree of similarity between the statistical properties of the synthesized and flight data. To illustrate this point, Figure 15 compares the autocorrelation of an unfiltered probe-pressure time trace for synthesized and HARV flight data using data from Case 4. The autocorrelation describes the general dependence of data values at one point in time on the values at another time[8,9]. Details on the calculation of the autocorrelation and other random data analysis techniques can be found in Reference 8. The autocorrelogram will always have a value of one at zero time lag. That is to say, any value is perfectly correlated with itself. For wide band random noise, the autocorrelation will rapidly decrease as the time lag is increased. This indicates decreasing dependence of the values from some specified earlier point in time as the time lag increases.

The autocorrelogram of the unfiltered flight data shows a steady decrease in the autocorrelation until a time lag of 15 scans is reached. After this point, the data have no meaningful dependence on any scan

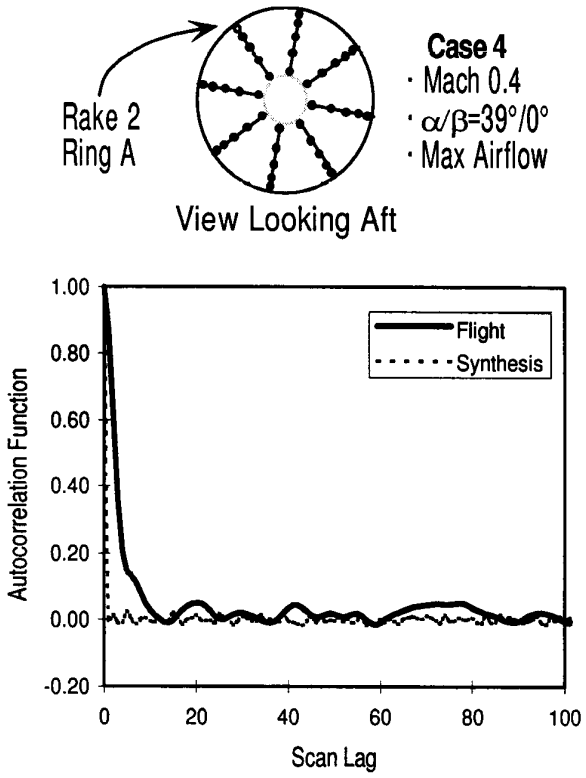

Figure 15. Autocorrelagrams of Unfiltered Flight and Synthesized Time Histories

preceding it by more than 15 scans. Considering then the autocorrelation of the synthesized data, it is evident that no scan has any dependence on any preceding scan. The autocorrelation is one at zero time lag, as it should, however the very next scan is seen to have a nearly zero autocorrelation. This indicates a distinctively different character between the flight and synthesized data. Theoretically, the synthesized data will permit two adjacent scans to vary between the maximum and minimum pressure values within the entire time trace. Even on an intuitive level, this clearly is not possible for naturally occurring pressure data. This is one of the primary reasons digital filtering is introduced into the synthesis process.

Power spectra provide another description of how the synthesized and flight data time histories may differ. Figure 16 illustrates power spectral densities (PSD) for the flight and synthesized data prior to digital filtering. The PSD for the synthesized data is flat across the frequency spectrum, indicating white noise with no preferred frequency bands. This is to be expected with a signal produced from a normally distributed random number generator. The PSD of the flight data indicates a roll off characteristic produced by the on-board six-pole Butterworth analog filter. This filter has a cut off frequency of 400 Hz, and is designed to prevent aliasing of the digitized data. This PSD is the result of the basic character of the measured data combined with the roll off characteristics of the analog filter. This difference in the unfiltered PSDs suggests a potential improvement to the synthesis methodology. By pre-filtering the synthesized data with a digital filter simulating the analog anti-aliasing filter, a character more closely matching the flight data can be imposed on the results of the random number generator.

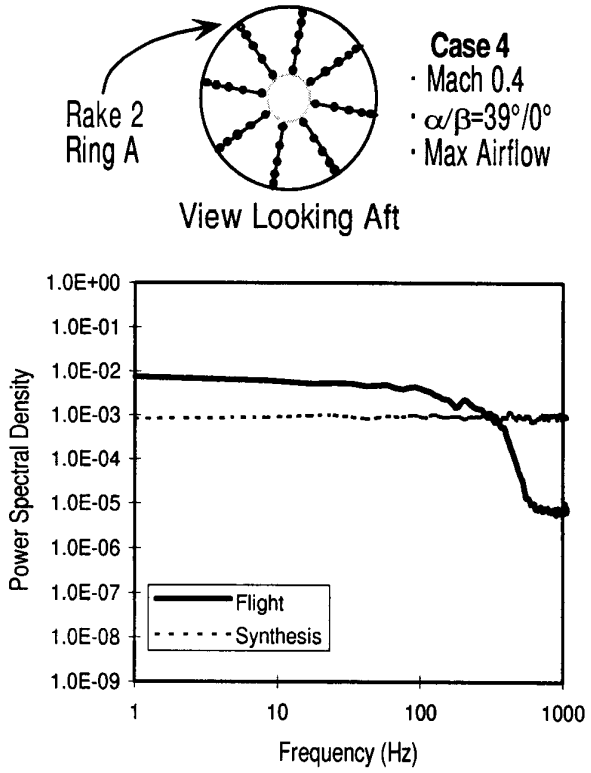

Figure 16. Power Spectral Density of Unfiltered Flight and Synthesized Time Histories

Digital Filtering

Introduction of a filter into the synthesized data imposes a degree of dependency for time lags within the window width of the filter. Because digital filters use some sort of averaging scheme within a sliding window of fixed width, a filtered scan will "feel" the influence of its neighboring scans within the filter window. The autocorrelogram of the filtered synthesized and flight data signals is shown in Figure 17. The synthesized data show a positive correlation for scan lags up to nine scans, the width of the filtering window. This is less than the 15 scan lag of the flight data; however, the character of the synthesized data more closely matches that of the flight data. This illustrates how the digital filter prevents the synthesized data from varying between maximum and minimum pressure values within adjacent scans.

Post-filtered time histories of synthesized and flight data exhibit more similar power spectral characteristics than the unfiltered data discussed above. Figure 18 illustrates the post-filtered comparisons. The roll off characteristics are similar between the two. The synthesized data show higher energy content in the upper frequency bands because its prefiltered data, shown in Figure 16, had higher energy levels than the flight data, in part due to the analog filtering imposed on the flight data. The recurring lobes in the higher frequencies of the filtered synthesized and flight data are artifacts of the nine scan sliding average digital filter used for the HARV program. This type of filter matches the characteristics of a 100 Hz cutoff, five-pole Bessel filter up to about 200 Hz. However, this simplified digital filter introduces some relative amplification in frequency bands above 200 Hz.

The DDS code, like other synthesis procedures, assumes the time variant pressure data to be normally distributed. This assumption was checked by computing probability density functions for the synthesized

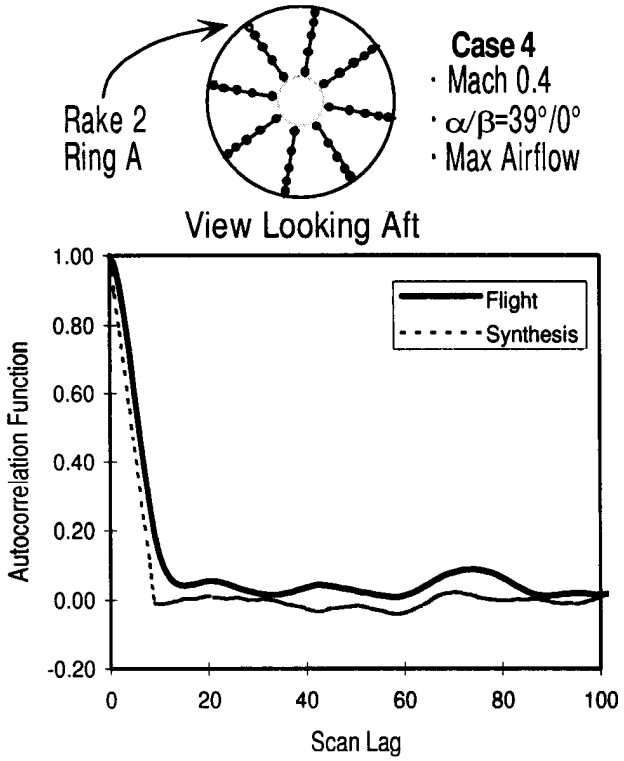

Figure 17. Autocorrelograms of Digitally Filtered Flight and Synthesized Time Histories

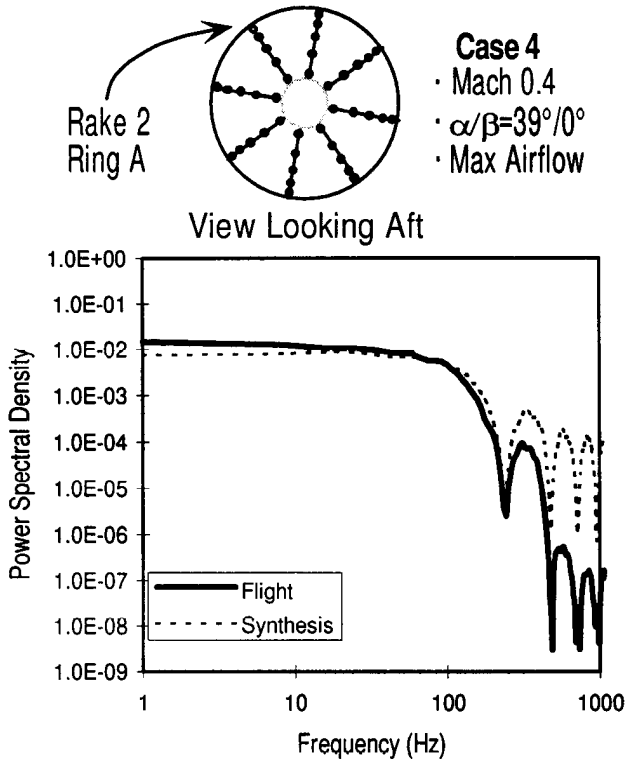

Figure 18. Power Spectral Density of Filtered Flight and Synthesized Time Histories

and HARV flight test data. Post-filtered traces were used in both cases. Analysis was performed on a sampling of probes, and a representative case is shown in Figure 19. In both cases, the distributions of time variant data are very nearly Gaussian. This result is in agreement with those of previous researchers[10,11]. This level of agreement was achieved on a high airflow case at Mach 0.4. Other flight conditions and power settings may not produce similar agreement. For example, high subsonic Mach numbers at low inlet airflows or inlet buzz conditions will introduce a periodic characteristic into the time variant pressure data, which invalidates the Gaussian assumption.

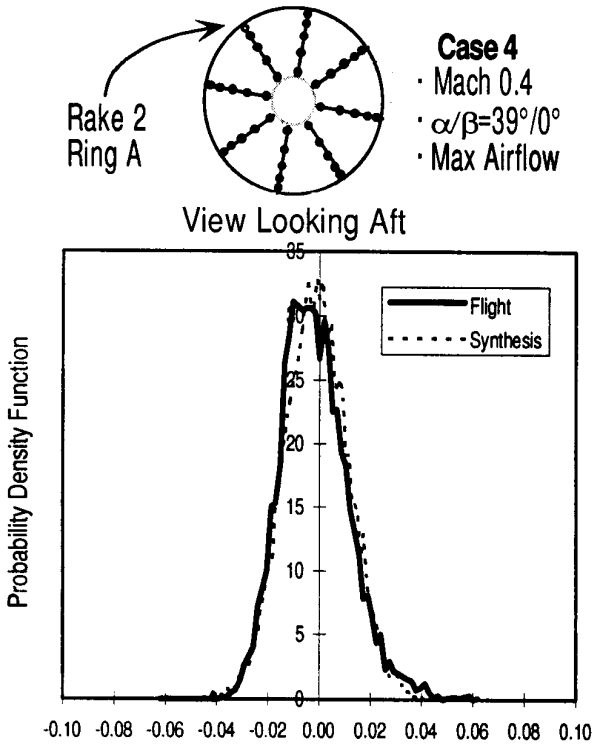

Figure 19. Probability Density Function for Filtered Flight and Synthesized Data

Pattern Averaging

Pattern averaging was introduced by Sedlock[1] after he found a significant improvement in distortion synthesis predictions with the technique. He suggests that since each distortion synthesis prediction is determined by a different set of random numbers, each prediction will be unique. For each probe, he considered the predicted pressure at peak distortion to be part of a distribution. An average peak distortion pattern is obtained by repeating the solution several times with different sets of random numbers. The individual probe pressures at each peak are then averaged to obtain the most probable maximum pressure distortion pattern. The DDS results shown here were computed using an average of six peak distortion patterns.

In practice, very erratic peak patterns are obtained without pattern averaging. This is attributed to the random number generator producing time traces within a single pattern that are truly independent from each other. In reality, probes in close proximity to each other will be correlated to a certain degree. The filtering process imposes some autocorrelation within each probe time trace. However, it does not impose any cross correlation between probes. Cross correlation for two sets of data describes the dependence of one set on the other at different time lags[8]. Figure 20 shows a cross correlation between

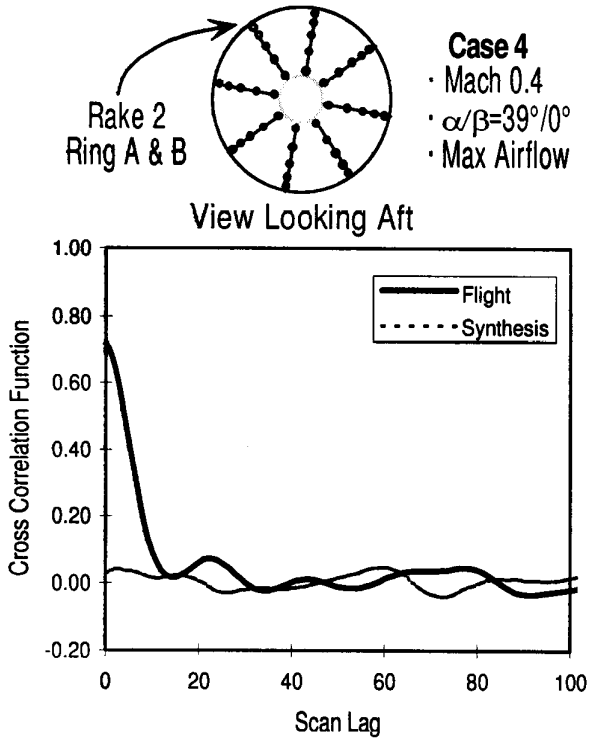

Figure 20. Cross Correlation Between Adjacent Probes
Post-Filtered Data

two adjacent probes on the AIP for synthesized and flight data. The figure illustrates how the flight data exhibit a significant degree of correlation between the probes for time lags less than 15 scans. As one would expect from the random number generator the synthesized data show no cross correlation. As the distance between probes increases, the cross correlation between probes decreases. As shown in Figure 21, there is virtually no correlation between two probes on opposite sides of the AIP for the flight or synthesized data.

The pattern averaging process appears to impose a degree of spatial correlation on the peak dynamic pattern prediction. While it does not actually change any of the probe time histories, it does significantly alter the predicted peak pattern prediction in a way that better simulates flight data.

DISTORTION PREDICTION RESULTS

Peak dynamic distortion prediction using the combined CFD/synthesis approach was generally biased high. The predictions were conservative, yielding results higher than the flight measured data. Comparisons of peak circumferential distortion intensity using GEAE's $(\Delta P/P_c)_{max}$ parameter[12] for the Mach 0.4 cases are shown in Figure 22. The predictions are high by a nearly constant increment of 0.02. Likewise, radial distortion predictions are also high as shown in Figure 23. The codes do correctly predict a tip radial pattern in all cases.

Prediction of average RMS turbulence was within 1% of flight test values. CFD/synthesis results are compared with flight test data for Mach 0.4 in Figure 24. Turbulence trends with increasing angle of attack were well represented by the predictions. The turbulence pattern prediction for Case 4, Mach 0.4,

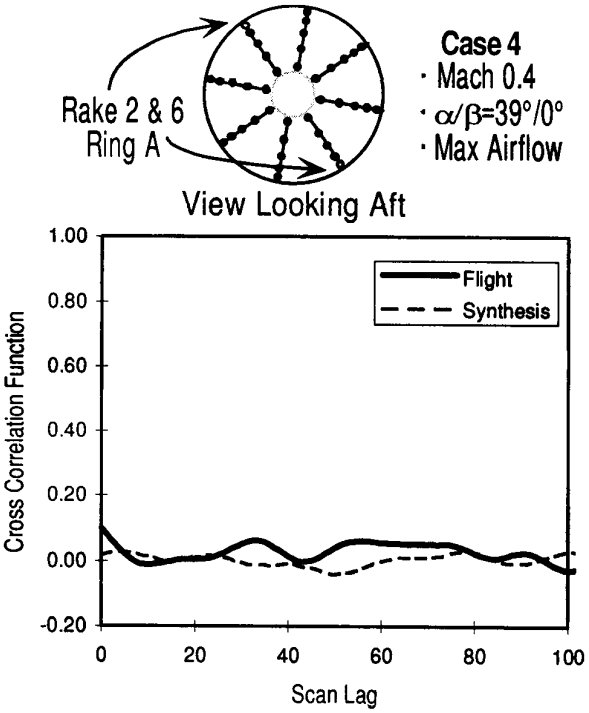

Figure 21. Cross Correlation Between Non-Adjacent Probes
Post-Filtered Data

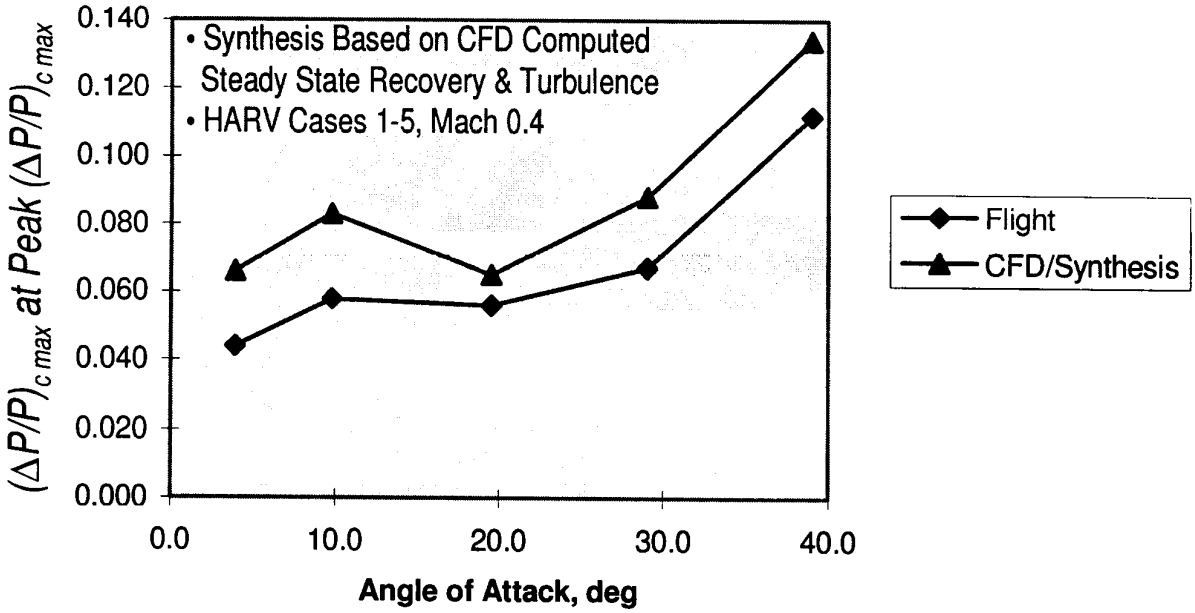

Figure 22. CFD/Synthesis Prediction of Peak Circumferential Distortion
Mach 0.4, Cases 1-5

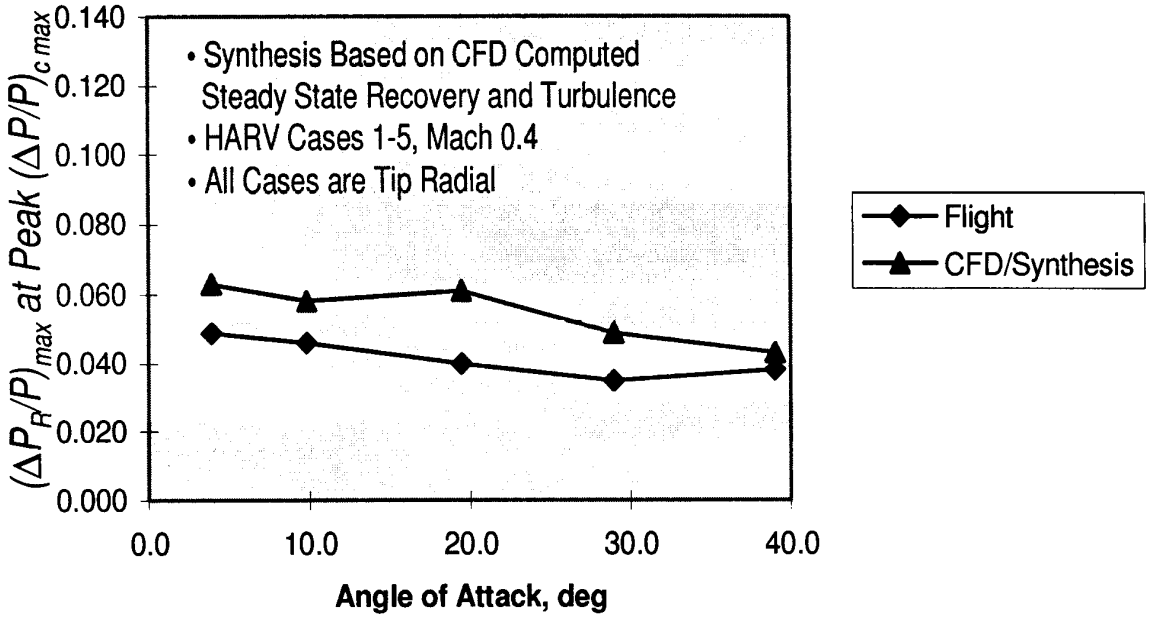

Figure 23. CFD/Synthesis Prediction of Dynamic Radial Distortion
Mach 0.4, Cases 1-5

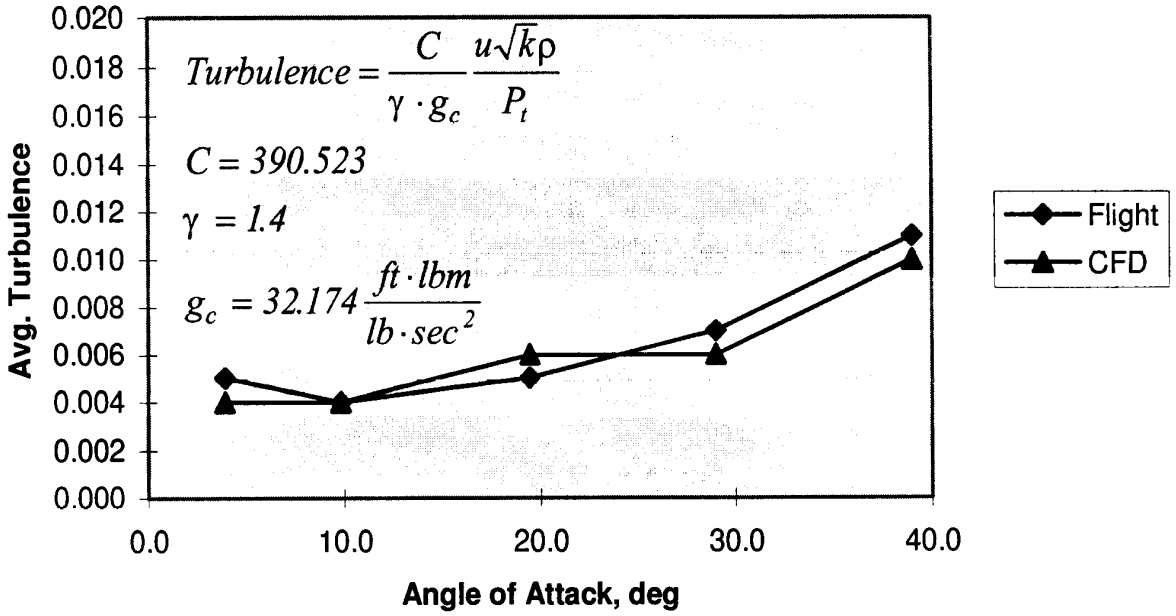

Figure 24. Turbulence Predictions Using CFD/Synthesis Methodology
Mach 0.4, Cases 1-5

α=40° is shown in Figure 25. The overall features of the pattern are fairly well predicted, but there are many specific details that are not correctly predicted.

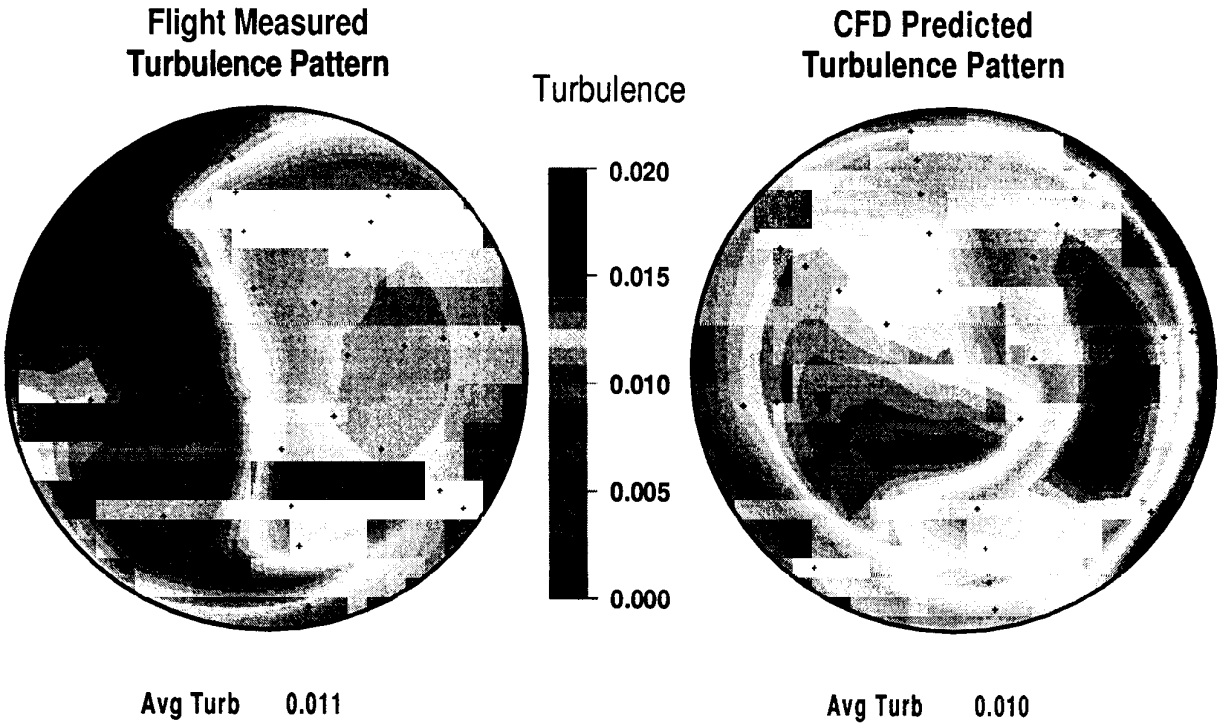

Figure 25. CFD Prediction of Turbulence Pattern
Mach 0.4, α=39°, Case 4 - View Looking Forward

Agreement between the flight and synthesized peak dynamic patterns varied somewhat but in general was good. A representative sample is shown in Figure 26 for the highest angle of attack considered, Case 4. As might be deduced from the distortion levels, the synthesized patterns exhibit minimum AIP total pressures below those of the flight data. In some cases the minimum pressure is clocked off a rake position from the flight test results. The overall features of the Case 4 pattern well represent the CFD/synthesis pattern prediction capability.

The validation portion of this effort examined three Mach 0.3 flight conditions. Cases 6-8 covered the 10° to 30° angle of attack range. Figure 27 shows the peak circumferential distortion predictions at Mach 0.3. These results are similar to the Mach 0.4 cases in that distortion levels are overpredicted, particularly at α=20°. The levels are in good agreement at α=10° and 30°. Peak radial distortion intensity was overpredicted also. As shown in Figure 28, there was a nearly constant increment of 0.02 between the flight test results and the CFD/synthesis predictions.

The bias in the predictions is attributed to over prediction of steady state total pressure losses in separated and vortical regions of the inlet flowfield. This conclusion is based on several observations. First, the synthesis procedure, when checked out using flight measured steady state recovery and turbulence, yields good agreement with flight measured peak distortion data. Next, the overall prediction of the average turbulence at the AIP is in line with flight test measurements. This, coupled with unpublished observations from other researchers showing that specifics of the turbulence pattern do not have a first order impact on dynamic distortion, indicates the turbulence pattern prediction is not the prime contributor. Finally, the CFD solution clearly underpredicts the steady state recovery loss in separated and vortical flow regions as illustrated in Figure 13. These reduced local total pressure recoveries propagate

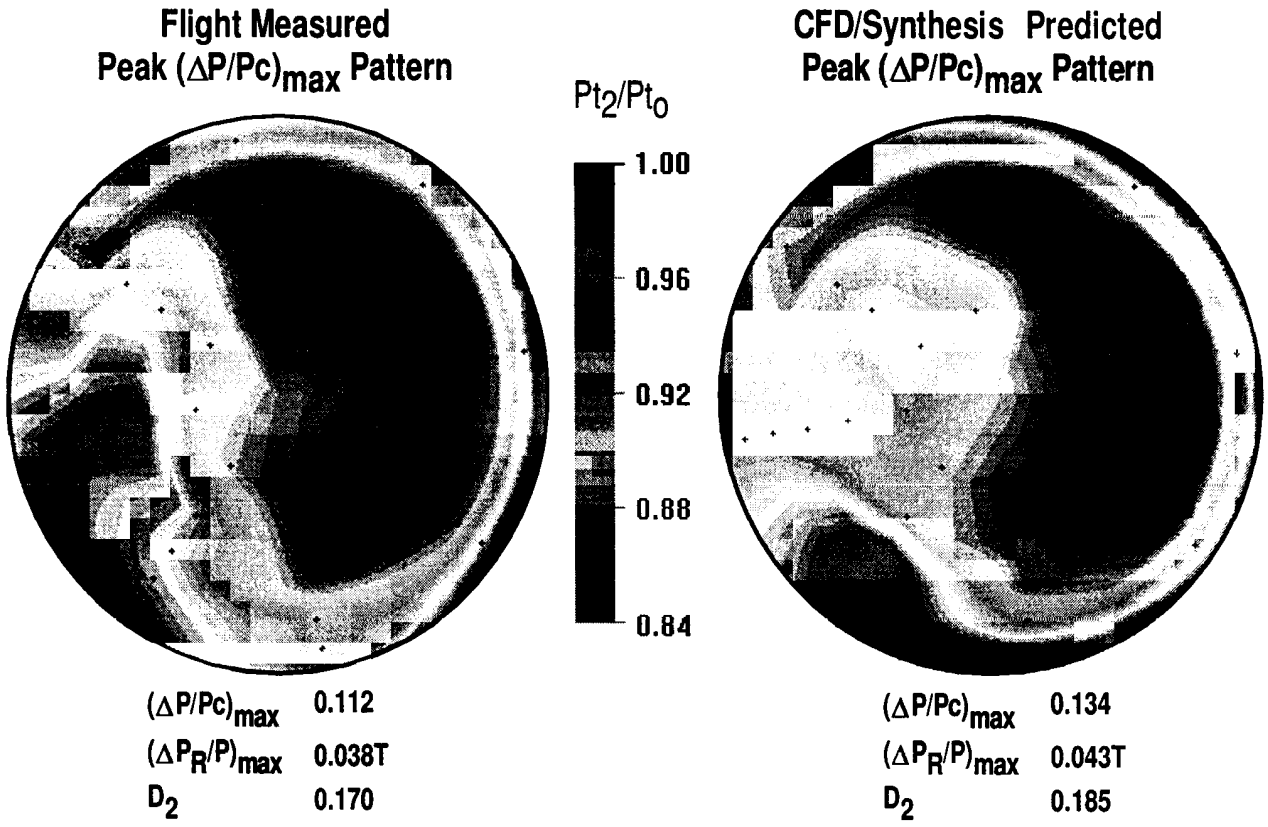

Figure 26. CFD/Synthesis Prediction of Peak Circumferential Distortion Pattern
Mach 0.4, α=39°, Case 4 - View Looking Forward

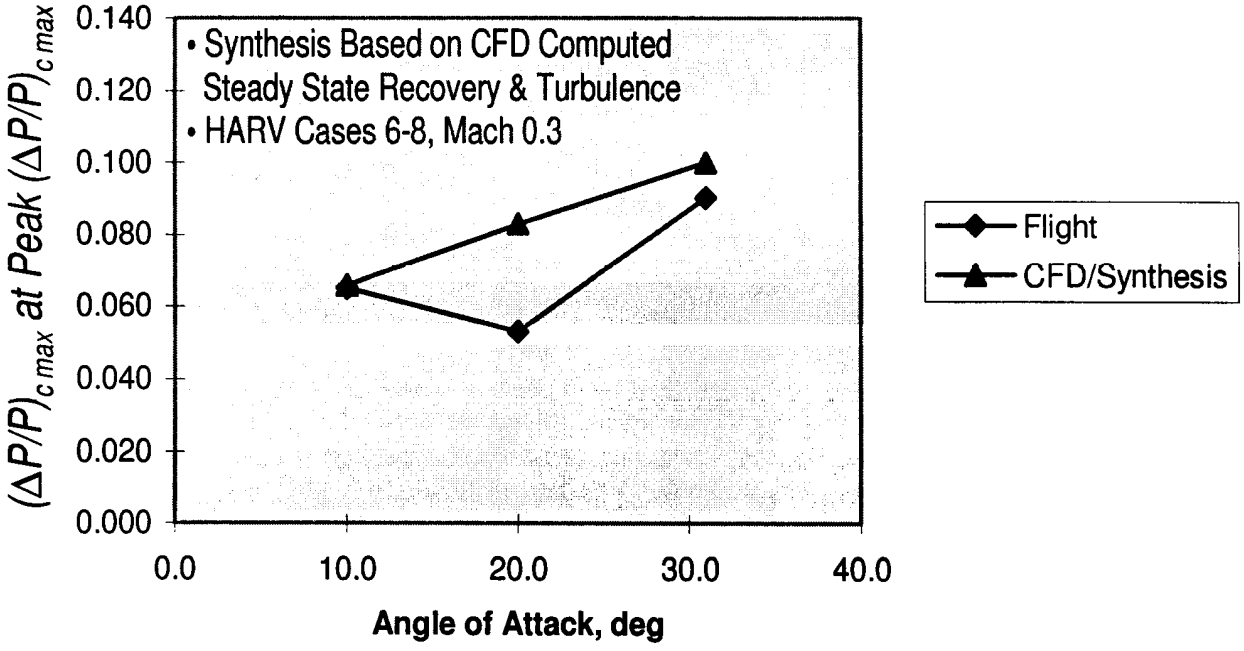

Figure 27. CFD/Synthesis Prediction of Peak Circumferential Distortion
Mach 0.3, Cases 6-8

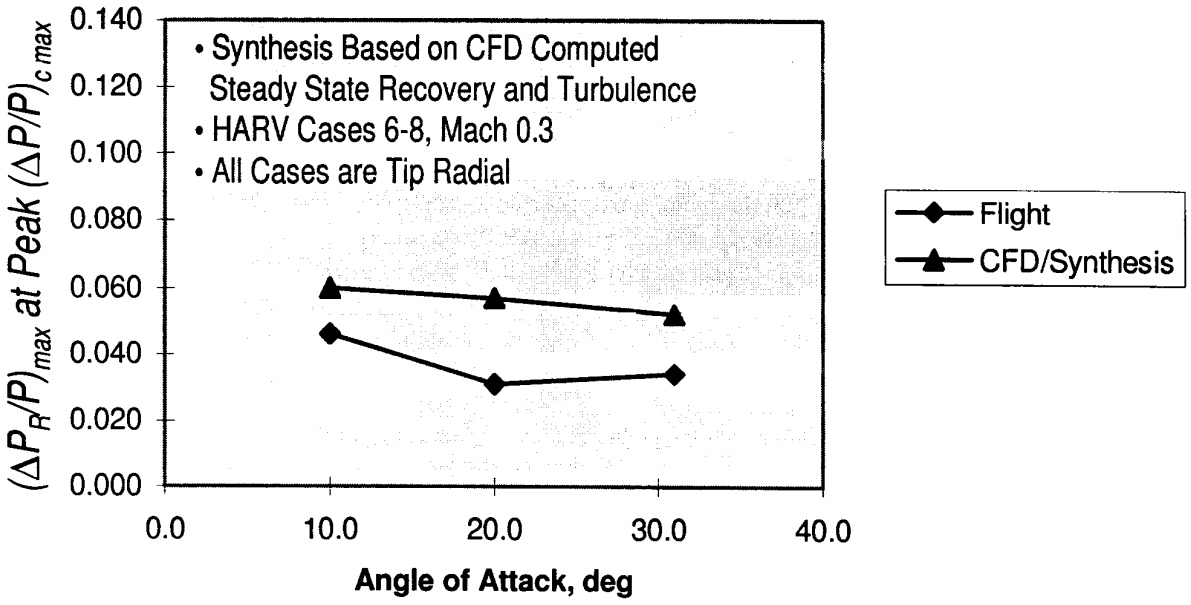

Figure 28. CFD/Synthesis Prediction of Dynamic Radial Distortion
Mach 0.3, Cases 6-8

through the CFD/synthesis process until they manifest themselves as an over prediction of peak dynamic distortion.

While the current procedure does consistently overpredict peak dynamic distortion, it does yield useful distortion data. Overall distortion generating features are predicted, along with a conservative estimate of their impact on distortion levels. Furthermore, this study has identified specific areas for improvement which are already being addressed through follow-on efforts.

RECOMMENDATIONS

Completion of this baseline study provides an opportunity to consider follow-on efforts to further understand the complicated inlet aerodynamics of inlet CFD and improve its predictive capability. Many areas could be explored further in near and far-term efforts. A listing of near-term efforts has been generated. These areas of possible enhancement include F/A-18 inlet CFD improvements, synthesis methodology robustness, and the expanded distortion prediction envelope. These areas of improvement have received approval for a follow-on CFD study by NASA and are currently in work at McDonnell Douglas.

The F/A-18 inlet CFD improvements will concentrate on improving the baseline CFD grid and methodology. This will be done by extending the C grid around the periphery of the entire inlet lip, increasing grid density in regions of flow separation, evaluating grid block interfaces to ensure information is being transferred across zone boundaries, and enhancing vortex generator modeling. A reexamination of the full-scale aircraft will also be performed to assess what, if any, pertinent features should be added to the baseline grid. The engine face boundary conditions will also be assessed to determine if alternative means

can be used to better simulate engine operating influences within the duct. The eight original HARV flight conditions will be reprocessed through the CFD methodology with all selected improvements to assess whether increased predictive capability has been achieved.

The synthesis methodology robustness effort will assess the robustness of the random number generator (RNG) in the baseline methodology. Further statistical analysis will be performed on the synthesized time traces to determine the degree to which the RNG models the behavior of the dynamic flowfield at the HARV aerodynamic interface plane (AIP). Comparisons between the statistical analysis of the CFD synthesized and the HARV flight measured time traces will be performed. Recommendations for any appropriate improvements to the RNG methodology will be made. A potential improvement may involve pre-filtering the synthesized data using a digital version of the on-board analog filter to impose an additional degree of realism on the synthesized time traces.

The expanded distortion prediction envelope task will push the CFD code into areas of higher levels of inlet distortion and turbulence. This effort will include seven new HARV flight conditions. These conditions will include α's beyond 40°, non-zero β conditions, takeoff maneuvers, and higher aircraft Mach numbers up to 0.6. The CFD methodology will be reassessed at these more severe inlet conditions.

This follow-on effort may further improve the predictive capability of this inlet CFD methodology. Future far-term efforts should emphasize improvements in inlet turbulence modeling, vortex flow interaction modeling, engine flow modeling, and engine/inlet aerodynamic interactions. The future of inlet CFD modeling is promising at reducing aircraft development costs and time spans, and should continue to be explored.

SUMMARY

A procedure has been developed to estimate inlet dynamic distortion using CFD computed data. This procedure involves a combined approach of 1) obtaining a CFD steady state prediction of the diffuser flowfield, 2) the correlation of the computed data with RMS turbulence, and 3) generating estimates of the peak dynamic distortion using a synthesis approach. Blind predictions of the dynamic distortion for four flight conditions are in qualitative agreement with the flight test data and should become more accurate as the CFD predictions are improved. The excellent agreement between the predicted inlet lip static pressures and the flight test data indicate a good prediction of the boundary layer and secondary flow regions near the inlet lip. Predictions of the average total pressure recovery at AIP were within 1% of the flight test data for the eight simulated flight conditions. The predicted recovery patterns differ significantly at the higher angles of attack. This indicates the recovery loss mechanisms are being captured correctly by the CFD simulations (e.g., boundary layer development, strength of the vortices from the VG's, etc.) but the trajectories of these secondary flow features may not be predicted adequately. The CFD predicted minimum total pressures at the AIP are consistently lower than the flight test data which causes the predictions of dynamic distortion to be high in all cases.

Several assumptions were made to the geometry and boundary conditions which may significantly affect the CFD prediction of the flowfield at the AIP. The leading edge flap/fuselage junction was not rigorously modeled and could affect the inlet lip losses. No trailing edge flap was modeled although deflection angles were less than 5 degrees in all cases and should not significantly alter the wing circulation. Differences in the CFD predicted steady state recovery patterns at the AIP are most likely a result of unsatisfactory modeling of the vortex generators and the boundary condition employed at the extended diffuser exit and

engine influences at the AIP. The vortex generators in the CFD simulations were later found to be located 2.1 inches inboard of their correct position in the diffuser. The VG's were also modeled as flat plates; whereas, the actual HARV VG's are 8% thick airfoils. The surface of the VG's themselves were assumed inviscid which is thought to be a good assumption but will be investigated in the follow on task.

The downstream diffuser boundary condition is thought to be the most significant deficiency in the CFD simulation. The current assumption of downstream constant static pressure does not simulate the upstream running characteristics from the presence of the rotating fan. Recently, a new engine face model has been implemented in the NASTD code to model the compressor pumping characteristics which have been shown to alter the diffuser static pressure distribution and energize low momentum flow (raise the minimum recovery). This new technique involves the addition of an interface at the fan face which models a rotor process (work addition) and a stator process (isentropic turn). These processes have been defined based on the conservation of mass, energy, and polytropic relations to model losses.

These enhancements to the CFD modeling of the VG's and engine face may provide significantly better predictions of the recovery contour patterns at the AIP and may remove the necessity of "sorting" the turbulence data prior to generation of the correlation coefficient. Expanding the database used in developing the correlation coefficients to include higher Mach number and more extreme α and β cases should make the procedure more robust across the flight regime. Additional configurations in addition to the HARV will also extend the applicability of this method to a variety of aircraft and inlet types.

ACKNOWLEDGMENTS

The work reported here was funded by the NASA Dryden Flight Research Center and carried out at McDonnell Douglas Corporation, St. Louis, Missouri. The authors wish to thank Kevin Walsh and Frank W. Burcham Jr. of NASA Dryden for their interest and support of this research. The authors also wish to acknowledge the contributions of W. A. Yonke and A. B. Cain of McDonnell Douglas who provided valuable assistance in this effort.

REFERENCES

1. Sedlock, D., "Improved Statistical Analysis Method for Prediction of Maximum Inlet Distortion," AIAA 84-1274, June 1984.

2. Regenie, Victoria, Donald Gatlin, Robert Kempel, and Neil Matheny, *The F-18 High Alpha Research Vehicle: A High-Angle-of-Attack Testbed Aircraft*, NASA TM 104253, 1992.

3. Walsh, Kevin, Andrew J. Yuhas, William G. Steenken, John Williams, *Inlet Distortion for an F/A-18 Aircraft During Steady-Aerodynamic Conditions Up to 60° Angle of Attack*, NASA TM 104325, 1996.

4. Yuhas, Andrew J., Ronald J. Ray, Richard R. Burley, William G. Steenken, Leon Lechtenberg, and Don Thornton, *Design and Development of an F/A-18 Inlet Distortion Rake: A Cost and Time Saving Solution*, NASA TM 4722, October 1995.

5. Bush, R. H., "A Three Dimensional Zonal Navier Stokes Code for Subsonic through Hypersonic Propulsion Flowfields," AIAA 88-2830, July 1988.

6. Spalart, P. R. and S. R. Allmaras, "A One-Equation Turbulence Model for Aerodynamic Flows," AIAA-92-0439, 1992.

7. Menter, Florian R., "Zonal Two Equation k-ω Turbulence Models for Aerodynamic Flows," AIAA 93-2906, July 1993.

8. Bendat, J. S. and A. G. Piersol, *Measurement and Analysis of Random Data*, John Wiley & Sons, 1966.

9. Crites, R. C. and M. V. Heckart, "Application of Random Data Techniques to Aircraft Inlet Diagnostics," AIAA 70-597, May 1970.

10. Stevens, C. H., E. D. Spong and R. C. Oliphant, " Evaluation of a Statistical Method for Determining Peak Inlet Flow Distortion Using F-15 and F-18 Data," AIAA 80-1109, June 1980.

11. Jacocks, J. L., "Statistical Analysis of Distortion Factors," AIAA 72-1100, November 1972.

12. Williams, John G., William G. Steenken, and Andrew J. Yuhas, "*Estimating Engine Airflow in Gas Turbine-Powered Aircraft with Clean and Distorted Inlet Airflows*," NASA CR 186036, 1996.

REPORT DOCUMENTATION PAGE

Form Approved
OMB No. 0704-0188

Public reporting burden for this collection of information is estimated to average 1 hour per response, including the time for reviewing instructions, searching existing data sources, gathering and maintaining the data needed, and completing and reviewing the collection of information. Send comments regarding this burden estimate or any other aspect of this collection of information, including suggestions for reducing this burden, to Washington Headquarters Services, Directorate for Information Operations and Reports, 1215 Jefferson Davis Highway, Suite 1204, Arlington, VA 22202-4302, and to the Office of Management and Budget, Paperwork Reduction Project (0704-0188), Washington, DC 20503.

1. AGENCY USE ONLY (Leave blank)	2. REPORT DATE	3. REPORT TYPE AND DATES COVERED
	September 1996	Contractor Report

4. TITLE AND SUBTITLE

Dynamic Inlet Distortion Prediction with a Combined Computational Fluid Dynamics and Distortion Synthesis Approach

5. FUNDING NUMBERS

WU 505-69-30

6. AUTHOR(S)

W.P. Norby, J.A. Ladd, and A.J. Yuhas

7. PERFORMING ORGANIZATION NAME(S) AND ADDRESS(ES)

McDonnell Douglas Aerospace
P. O. Box 516
St. Louis, MO 63166

AS&M, Inc.
P. O. Box 273
Edwards, CA 93523

8. PERFORMING ORGANIZATION REPORT NUMBER

N/A

9. SPONSORING/MONITORING AGENCY NAME(S) AND ADDRESS(ES)

Sponsoring Agency:
NASA Lewis Research Center
21000 Brookpark Road
Cleveland, OH 44135-3191

Monitoring Agency:
NASA Dryden Flight Research Center
P. O. Box 273
Edwards, CA 93523-0273

10. SPONSORING/MONITORING AGENCY REPORT NUMBER

CR-198053
(H-2129)

11. SUPPLEMENTARY NOTES

Dryden Technical Monitor: Kevin Walsh. W.P. Norby and J.A. Ladd, McDonnell Douglas Aerospace, St. Louis, Missouri, and A.J. Yuhas, AS&M, Inc., Hampton, Virginia. Presented at the High-Angle-of-Attack Technology Conference, NASA Langley Research Center, Hampton, Virginia, Sept. 17–19, 1996.

12a. DISTRIBUTION/AVAILABILITY STATEMENT

Unclassified—Unlimited
Subject Category 07

12b. DISTRIBUTION CODE

13. ABSTRACT (Maximum 200 words)

A procedure has been developed for predicting peak dynamic inlet distortion. This procedure combines Computational Fluid Dynamics (CFD) and distortion synthesis analysis to obtain a prediction of peak dynamic distortion intensity and the associated instantaneous total pressure pattern. A prediction of the steady state total pressure pattern at the Aerodynamic Interface Plane is first obtained using an appropriate CFD flow solver. A corresponding inlet turbulence pattern is obtained from the CFD solution via a correlation linking root mean square (RMS) inlet turbulence to a formulation of several CFD parameters representative of flow turbulence intensity. This correlation was derived using flight data obtained from the NASA High Alpha Research Vehicle flight test program and several CFD solutions at conditions matching the flight test data. A distortion synthesis analysis is then performed on the predicted steady state total pressure and RMS turbulence patterns to yield a predicted value of dynamic distortion intensity and the associated instantaneous total pressure pattern.

14. SUBJECT TERMS

Computational fluid dynamics, Distortion synthesis, F/A-18 airplane, Inlet, Inlet distortion

15. NUMBER OF PAGES

39

16. PRICE CODE

AO3

17. SECURITY CLASSIFICATION OF REPORT	18. SECURITY CLASSIFICATION OF THIS PAGE	19. SECURITY CLASSIFICATION OF ABSTRACT	20. LIMITATION OF ABSTRACT
Unclassified	Unclassified	Unclassified	Unlimited

Available from the NASA Center for AeroSpace Information, 800 Elkridge Landing Road, Linthicum Heights, MD 21090; (301)621-0390